Monthly Notices of the ROYAL ASTRONOMICAL SOCIETY

MNRAS **526,** 717–739 (2023) https://doi.org/10.1093/mnras/stad2750
Advance Access publication 2023 September 23

Into the Mystic: ALMA ACA observations of the Mystic Mountains in Carina

Megan Reiter [1]★, P. D. Klaassen [2], L. Moser-Fischer,[3] A. F. McLeod [4,5] and D. Itrich [6]

[1]*Department of Physics and Astronomy, Rice University, 6100 Main Street - MS 108, Houston, TX 77005, USA*
[2]*The UK Astronomy Technology Centre, Royal Observatory Edinburgh, Blackford Hill, Edinburgh EH9 3HJ, UK*
[3]*University of Bonn, Argelander-Institut fuer Astronomie, European ALMA Regional Centre – German node, Auf dem Huegel 71, D-53121 Bonn, Germany*
[4]*Centre for Extragalactic Astronomy, Department of Physics, Durham University, South Road, Durham DH1 3LE, UK*
[5]*Department of Physics, Institute for Computational Cosmology, University of Durham, South Road, Durham DH1 3LE, UK*
[6]*European Southern Observatory, Karl-Schwarzchild-Strasse 2, D-85748 Garching bei München, Germany*

Accepted 2023 August 27. Received 2023 August 21; in original form 2023 March 31

ABSTRACT

We present new observations of the Mystic Mountains cloud complex in the Carina Nebula using the ALMA Atacama Compact Array (ACA) to quantify the impact of strong UV radiation on the structure and kinematics of the gas. Our Band 6 observations target CO, ^{13}CO, and C^{18}O; we also detect DCN J=3–2 and ^{13}CS J=5–4. A dendrogram analysis reveals that the Mystic Mountains are a coherent structure, with continuous emission over $-10.5\,\mathrm{km\,s^{-1}} < \mathrm{v} < -2\,\mathrm{km\,s^{-1}}$. We perform multiple analyses to isolate non-thermal motions in the Mystic Mountains including computing the turbulent driving parameter, b, which indicates whether compressive or solenoidal modes dominate. Each analysis yields values similar to other pillars in Carina that have been observed in a similar way but are subject to an order of magnitude less intense ionizing radiation. We find no clear correlation between the velocity or turbulent structure of the gas and the incident radiation, in contrast to other studies targeting different regions of Carina. This may reflect differences in the initial densities of regions that go on to collapse into pillars and those that still look like clouds or walls in the present day. Pre-existing over-densities that enable pillar formation may also explain why star formation in the pillars appears more evolved (from the presence of jets) than in other heavily irradiated but non-pillar-like regions. High resolution observations of regions subject to an array of incident radiation are required to test this hypothesis.

Key words: stars: formation – HII regions – ISM: kinematics and dynamics – ISM: jets and outflows – Herbig–Haro objects.

1 INTRODUCTION

Feedback is the principal process by which molecular clouds are destroyed (Matzner 2002). High-mass stars inject energy and momentum into their surroundings via winds and radiation before their eventual deaths as supernovae. Growing evidence suggests that pre-supernova feedback plays a dominant role reshaping the interstellar medium (ISM) and regulating star formation (e.g. Kruijssen et al. 2019; McLeod et al. 2021; Chevance et al. 2022). Feedback has also been invoked as the stimulus for the formation of new stars, either by stimulating the collapse of existing cores or collecting material into new ones (e.g. Elmegreen & Lada 1977; Bertoldi 1989).

Many theoretical models have been developed to address the question of how stellar feedback shapes the surrounding gas. Models can produce dust pillars like those seen in many H II regions (e.g. Hester et al. 1996) either through growing instabilities or by revealing pre-existing substructure (e.g. filaments and cores) as the surrounding, lower-density material is more easily swept away (Gritschneder et al. 2010; Dale, Ercolano & Bonnell 2012; Tremblin et al. 2012a, b; Walch et al. 2013; Menon, Federrath & Kuiper 2020). Despite their morphological similarities, models predict differences in the following: density contrasts between the pillars and the surrounding medium, progression speeds of the ionization front, star formation efficiencies, and time-scales, particularly whether cores are already present or formed by the ionization-driven shock. This results in measurable differences in the gas kinematics within (and around) the photodissociation region (PDR) interface.

Despite the diagnostic potential of cold gas kinematics, only a few studies exist with high spatial resolution to measure the variation of the cold gas kinematics in dust pillars in star-forming regions. Far-IR observations from SOFIA and *Herschel* provide kinematic evidence for dust pillars forming via collapse on the edges of H II regions and small globules produced by turbulent fragmentation (Schneider et al. 2012; Tremblin et al. 2013). However, it is only with millimeter interferometry that dust pillars can be spatially and spectrally resolved. One of the first such studies was Klaassen et al. (2014) who mapped a pillar in Vulpecula. The observed pillar properties are most consistent with models that have low velocity dispersions, but no one model matches all of the observed gas kinematics (e.g. Gritschneder et al. 2009, 2010; Dale et al. 2012).

To probe a broader range of conditions, Klaassen et al. (2020) presented a survey of 13 dust pillars in the Carina Nebula that sample

★ E-mail: megan.reiter@rice.edu

Table 1. Spectral and imaging characteristics of the data.

Name	Frequency [GHz]	Bandwidth [MHz]	Resolution [km s^{-1}]	$\theta_{\rm min}$ [″]	$\theta_{\rm max}$ [″]	P.A. [°]	rms [mJy bm^{-1}]	Comment
				Molecular lines				
SiO J=5–4	217.1049800	468.75	0.337	5.39	7.18	87.6	100.3	not detected
DCN J=3–2	217.23855	468.75	0.337	5.39	7.18	87.6	100.3	in SiO spectral window
C^{18}O J=2–1	219.5603568	117.19	0.167	5.35	7.09	85.9	141.8	
^{13}CO J=2–1	220.3986765	117.19	0.167	5.30	7.04	86.9	245.4	
^{12}CO J=2–1	230.538	117.19	0.159	5.07	6.77	87.0	993.0	
^{13}CS J=5–4	231.220686	117.19	0.158	5.02	6.77	87.5	242.3	
				Continuum				
B6	225.8799	2530.0	40.038	4.95	6.75	86.9	1.700*	

Note. * RMS of the aggregated bandwidth image.

a range of morphologies and environments, including the incident ionizing flux. Many of these reside in the actively star-forming South Pillars where star formation may have been triggered by the hundreds of O- and B-type stars in the region (Smith et al. 2010b; Berlanas et al. 2023). Cold gas kinematics are broadly consistent with pillars forming from turbulent media as they are sculpted by ionizing radiation. However, this sample does not include the most intense ionizing radiation that affects the gas nearest the central clusters of Carina.

To probe the most intense feedback in the Carina Nebula, we target a cloud complex that is heavily irradiated by the young, massive cluster Trumpler 14 (Tr14). The so-called Mystic Mountains[1] (Area 29 in Hartigan et al. 2015) lie ∼1 pc to the north of Tr14. Copious ionizing photons ($Q_H \sim 10^{50}$ s^{-1}; Smith 2006a) illuminate and sculpt multiple pillars in the Mystic Mountains. Three famous Herbig–Haro (HH) jets emerge from the tips of these pillars – HH 901, HH 902, and HH 1066 (see Fig. 1 and Smith, Bally & Walborn 2010a; Reiter & Smith 2013, 2014). However, the pillars themselves are largely opaque and only a few protostars are detected in the infrared (IR; e.g. Povich et al. 2011; Ohlendorf et al. 2012). With modest angular resolution (∼2″), only the HH 1066 jet-driving source was directly detected in the infrared (Ohlendorf et al. 2012; Reiter, Smith & Bally 2016; Reiter et al. 2017). The HH 1066 driving source is also one of only two sources in Carina with a marginally resolved circumstellar disc (Mesa-Delgado et al. 2016). Reiter et al. (2017) argued that more intense feedback closer to Tr14 may have compressed the gas, leading to high densities that obscure the HH 901 and HH 902 jet-driving sources in the IR. Indeed, the first detections of the HH 901 and HH 902 driving sources were only recently reported by Cortes-Rangel et al. (2020).

In this paper, we present ALMA observations using the Atacama Compact Array (ACA; also known as the Morita Array) of the entire Mystic Mountains complex. The ionizing photon flux incident on the Mystic Mountains is an order of magnitude higher than the pillars in Klaassen et al. (2020). The complex is large (∼1′ × 2′), and thus samples a range of incident ionizing flux within a single pillar complex. By studying gas kinematics in the Mystic Mountain, we will constrain the role of ionizing radiation in stimulating or starving future star formation, a key test of the role of feedback in regulating star formation.

[1] as the region was dubbed when imaged to commemorate the 20th anniversary of the *HST*.

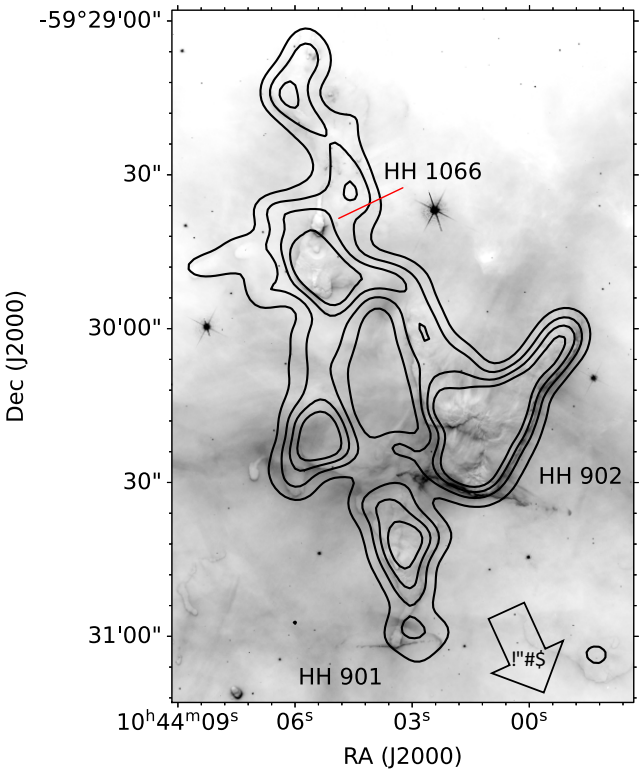

Figure 1. CO J=2–1 contours on an Hα image from *HST*. The famous jets, HH 901, HH 902, and HH 1066, are labelled. The CO emission is integrated over the velocity range $-10.5 < v < -2$ km s^{-1}; contours are 20, 40, 60, 80, and 100 per cent of the peak intensity.

2 OBSERVATIONS

ALMA ACA Band 6 observations of the Mystic Mountains were obtained on 2019 January 19. Observations are a mosaic of 21 pointings of the 7 m-array (12 antennae) mosaic centre RA=10$^{\rm h}$44$^{\rm m}$02$^{\rm s}$.010, Dec.=−59°30′01″.0 (ICRS). The maximum recoverable scale (MRS) is 28.6″. We also obtained Total Power (TP) data to ensure our observations capture emission from the largest scales. These were obtained on 2018 November 28–29 with a third epoch on 2018 December 04. Parameters of our observations are listed in Table 1.

Our observational setup targeted rotational transitions J=2–1 of the CO isotopologues ^{12}CO, ^{13}CO, and C^{18}O, as well as SiO J=5–

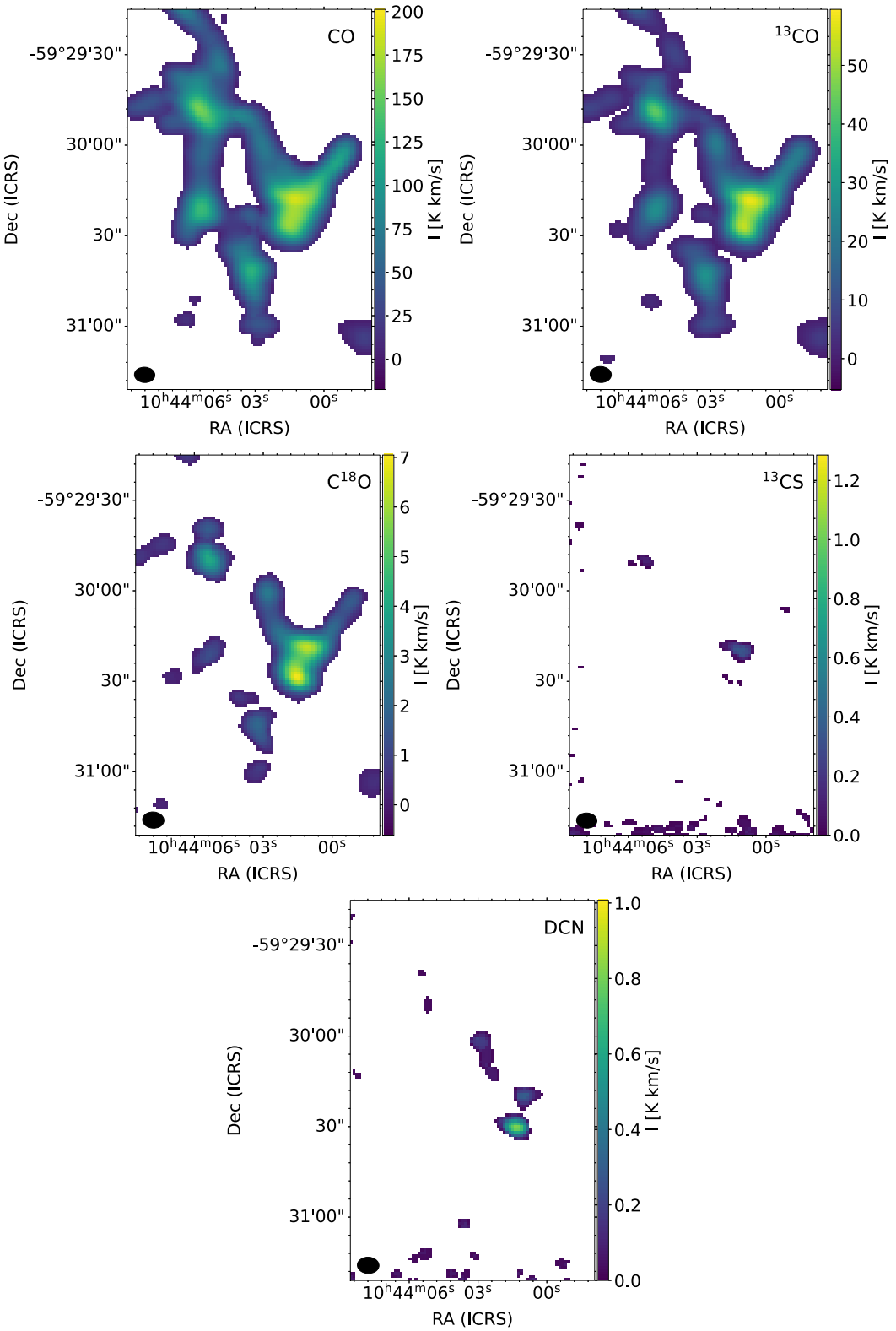

Figure 2. Integrated intensity (moment 0) maps of the lines detected in this study – CO, ^{13}CO, C^{18}O, ^{13}CS, and DCN. All CO isotopologues are detected with $>5\sigma$ significance; DCN and ^{13}CS are detected with $>3\sigma$ significance.

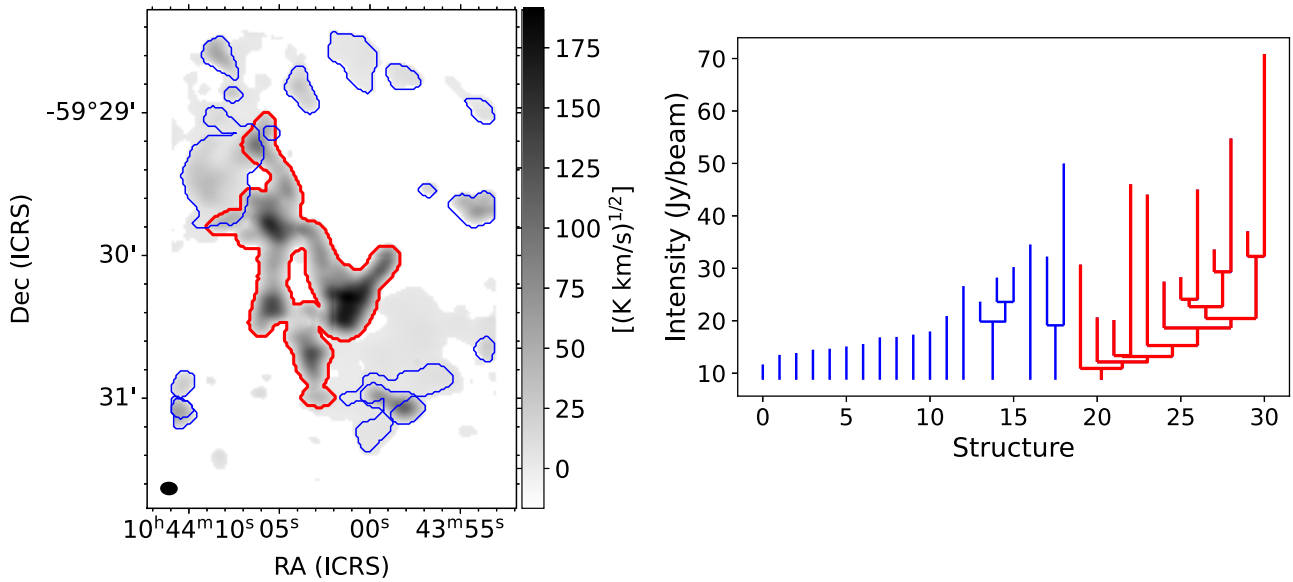

Figure 3. Applying a dendrogram analysis to the CO velocity cube ($-15 < v < 5\,\mathrm{km\,s^{-1}}$) shows the Mystic Mountains are a single, coherent structure. *Left:* shows the CO integrated intensity with coloured contours indicating dendrogram trunks. The Mystic Mountains is shown in red; all other features are shown in blue. *Right:* the dendrogram tree, using the same colour scheme as the left panel. The Mystic Mountains, shown in red, is a separate feature with all substructures stemming from the same trunk.

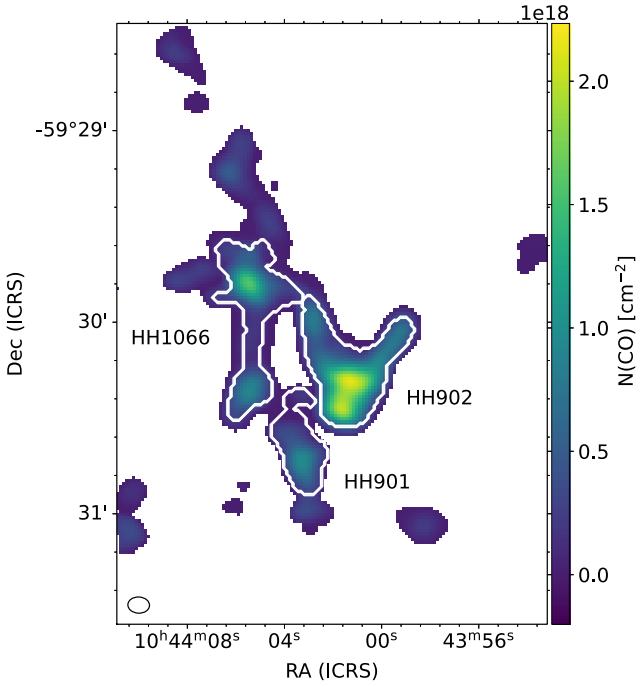

Figure 4. Column density map with a single white contour that outlines the branches identified by the CO dendrogram analysis. Peak and median values reported in Table 2 are computed within these pillar boundaries.

4 and ^{13}CS J=5–4. All observations were imaged to a velocity resolution 0.17 km s^{-1}. We also observed a continuum spectral window with resolution ∼40 km s^{-1}. When combined with line-free channels in other bands, continuum emission covers approximately 2.5 GHz in Band 6.

Bandpass, flux, and gain calibration were done with external calibrators using the *Common Astronomy and Software Applications* (CASA, McMullin et al. 2007) v5.4.0-70. The bandpass and flux calibrators for the Band 6 observations performed in January 2019 were J0940 − 6107 and J1047 − 6217.

Continuum subtraction and cleaning via the imaging pipeline yielded insufficient results for our needs, so continuum ranges were identified by eye and a deeper clean performed using `tclean` in CASA v6.4.4 to produce images. We applied automasking and Briggs-weighting with a robust parameter of 0.5. We deconvolved the image in multiscale mode with scale of 0, 5, and 15 times the pixel size of 1.0 arcsec. The absolute flux scaling uncertainty is estimated to be about 15 per cent. The synthesized beamsizes of the reduced data range typically between 5.″4 and 7.″2, corresponding to a spatial resolution 12 420–16 560 au at the distance of Carina (2.3 kpc; Smith 2006b; Göppl & Preibisch 2022).

Finally, the ACA and TP data were combined using the CASA task `feather`. This task regrids the lower resolution data to match the higher resolution data, scales them by the ratio of the clean beams, then combines the two data sets in fourier space before transforming back to the image plane. This provides much better recovery of extended emission than the ACA alone, allowing us to capture structures up to ∼27″ at 230 GHz (see Klaassen et al. 2020, for an example).

2.1 Complementary data from the *Hubble Space Telescope (HST)*

We compare the ALMA observations to a narrowband Hα image from *HST*. A four-point mosaic of the field containing HH 901, HH 902, and HH 1066, dubbed 'The Mystic Mountains,' was taken 2010 February 1–2 to commemorate the 20th anniversary of *HST* (PID 12050, P.I. M. Livio). Images were obtained with the UVIS channel of the Wide Field Camera 3 (WFC3). The total integration time in the F657N filter was 1980 s. The observations and their analysis are presented in more detail in Reiter & Smith (2013).

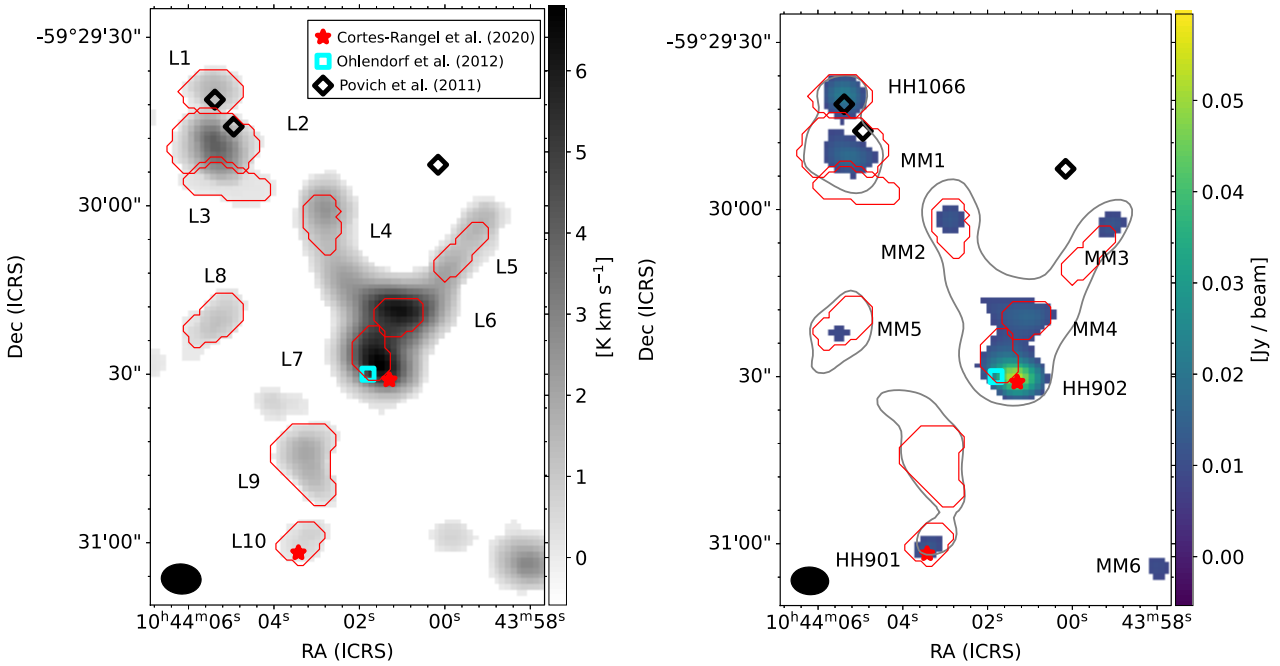

Figure 5. *Left:* local maxima (leaves) identified by the dendrogram analysis shown in red contours on a moment 0 map of $C^{18}O$. *Right:* dendrogram leaves (red contours) compared to continuum peaks shown in the colourscale. A single grey contour shows the $C^{18}O$ emission at 20 per cent of the peak emission. Both panels show YSOs detected in other surveys: black diamonds are YSOs from Povich et al. (2011); the cyan square is the point source from Ohlendorf et al. (2012); and the red stars are the YSOs identified by Cortes-Rangel et al. (2020).

3 RESULTS AND ANALYSIS

Fig. 2 shows the integrated intensity (moment 0) maps of all emission lines detected in this study. Extended CO emission traces the kinematics and cloud structure throughout the Mystic Mountains complex with knots of bright emission in ^{13}CO and $C^{18}O$ tracing $\sim 1-2$ clumps of emission in each pillar. The most complex emission is in the pillar with the HH 902 jet. Two emission peaks in the CO and isotopologues hint at multiple star-forming clumps.

Visual inspection of the CO datacube reveals that emission associated with the Mystic Mountains is contained within the velocity range $-15 < v < 5\,\mathrm{km\,s^{-1}}$. This range includes the systemic velocities of the HH 901 ($-5.0\,\mathrm{km\,s^{-1}}$) and HH 902 ($-8.5\,\mathrm{km\,s^{-1}}$) pillars identified by Cortes-Rangel et al. (2020). Pillar-like emission to the east and north of these two pillars contains HH 1066 (for which we estimate a systemic velocity of $-6.5\,\mathrm{km\,s^{-1}}$). Additional CO emission not associated with the Mystic Mountains is detected at other velocities ($\pm 20\,\mathrm{km\,s^{-1}}$ from the v_{LSR} of Carina, $-20\,\mathrm{km\,s^{-1}}$), but we do not discuss this further.

To determine the precise velocity range and extent of the gas associated with the Mystic Mountains complex, we use a dendrogram analysis to identify coherent structures in position–position–velocity space. As described in Rosolowsky et al. (2008) and Goodman, Pineda & Schnee (2009), dendrograms provide a hierarchical representation of data, aiding the analysis of physical conditions on multiple scales from a single data set. Large coherent features that are not part of another larger, parent structure are 'trunks'; these contain substructures called 'branches' that are composed of individual local maxima, or 'leaves,' that cannot be subdivided further.

We use the python packages ASTRODENDRO (Robitaille et al. 2019) and SCIMES (Colombo et al. 2015) to decompose the structures in the CO datacube. We use the following parameters for the decomposition: a minimum value (min_value) that defines the noise threshold – we adopt 6σ; a minimum intensity (min_delta) for that defines the threshold the peak flux must exceed to be identified as a separate structure – we adopt 2σ; and a minimum number of pixels for a leaf to be an independent entity – we use the number equivalent to three beams (124 pixels in our case).

With these parameters, a dendrogram analysis identifies the Mystic Mountains as a trunk, indicating that it is a coherent cloud complex with contiguous emission over the velocity range $-10.5 < v < -2\,\mathrm{km\,s^{-1}}$. Fig. 3 shows the Mystic Mountains as a single tree in red with other structures shown in blue. Within the Mystic Mountains complex, the dendrogram analysis identifies three separate pillars as branches. Contours defining the outlines of these branches are shown in Fig. 4. We refer to the pillars by the name of the prominent jets that they host – HH 901, HH 902, and HH 1066.

In the following sections, we use this velocity range to derive the spatially resolved physical parameters of the cold molecular gas in the Mystic Mountains. We provide maps of these spatially resolved quantities in Appendices A and B. To provide representative values in Table 2, we compute the values within the dendrogram branches that define each of the pillars.

3.1 Optical depth

We compute the optical depth at each position and velocity where emission is detected with a significance $\geq 5\sigma$ using the following expression (equation 1 from Choi, Evans & Jaffe 1993):

$$\frac{T_{\mathrm{main,v}}}{T_{\mathrm{iso,v}}} = \frac{1-e^{-\tau_{\mathrm{main,v}}}}{1-e^{-\tau_{\mathrm{iso,v}}}} = \frac{1-e^{-\tau_{\mathrm{main,v}}}}{1-e^{-\tau_{\mathrm{main,v}}/R}}, \quad (1)$$

where 'main' is the more abundant species and 'iso' is the optically thin (isotopologue) transition used to correct it. R is the scale factor for the relative abundance of the two species. We use

Table 2. Summary of molecular line derived physical properties. Columns are the species/transition, peak and median intensities, median column density if optically thin, median optical depth, and median column if optically thick, respectively. Spatially resolved maps of these quantities are shown in Appendices A–B.

Line	I_{peak} [K km s^{-1}]	I_{median} [K km s^{-1}]	$\log(N_{thin})_{max}$ [cm^{-2}]	$\log(N_{thin})_{median}$ [cm^{-2}]	τ_{max}	$\log(N_{thick})_{peak}$ [cm^{-2}]	$\log(N_{thick})_{median}$ [cm^{-2}]
Mystic Mountains; $v_{LSR} \approx -6.7$ km s^{-1} ‡							
^{12}CO J=2–1	185.0	46.5	17.0	16.2	44.6	18.3	17.2
^{13}CO J=2–1	57.5	8.8	16.5	15.4	4.2	16.6	15.5
C^{18}O J=2–1	6.9	1.14	15.6	14.8	–	–	–
HH 901 pillar; $v_{LSR} \approx -5.0$ km s^{-1} †							
^{12}CO J=2–1	114.2	38.8	16.8	16.4	33.0	18.0	17.5
^{13}CO J=2–1	27.0	9.0	16.1	15.7	0.68	16.1	15.7
C^{18}O J=2–1	1.97	0.61	15.0	14.5	–	–	–
HH 902 pillar; $v_{LSR} \approx -8.5$ km s^{-1} †							
^{12}CO J=2–1	174.1	65.6	17.0	16.6	44.6	18.3	17.9
^{13}CO J=2–1	56.8	18.3	16.5	16.0	1.9	16.6	16.0
C^{18}O J=2–1	6.90	1.84	15.6	15.0	–	–	–
HH 1066 pillar; $v_{LSR} \approx -6.5$ km s^{-1}							
^{12}CO J=2–1	138.9	42.0	16.9	16.6	35.0	18.2	17.6
^{13}CO J=2–1	42.1	7.65	16.4	15.7	3.1	16.4	15.8
C^{18}O J=2–1	4.03	0.81	15.3	14.7	–	–	–

Notes. † v_{LSR} from Cortes-Rangel et al. (2020)
‡ v_{LSR} from the intensity-weighted average velocity of the Mystic Mountains

[^{12}CO/^{13}CO]=60 (Rebolledo et al. 2016, see also Jacob et al. 2020) and [^{12}CO/C^{18}O]=560 (Wilson & Rood 1994). We assume the same excitation temperature for both molecules. We find that CO emission is optically thick over a large portion of the Mystic Mountains whereas ^{13}CO is only optically thick near the brightest emission in the HH 902 pillar. Maps of the spatially resolved optical depth at the source velocity are shown in Appendix A and maximum values are reported in Table 2.

3.2 Molecular column density

We compute the column density of each observed transition using the following equation (see e.g. Mangum & Shirley 2015):

$$N_{tot} = \frac{8\pi k\nu^2 Q(T_{ex}) e^{E_u/kT_{ex}} J_\nu(T_{ex})}{hc^3 g_u A_{ul}[J_\nu(T_{ex}) - J_\nu(T_{cmb})]} \int T_{mb} \frac{\tau_\nu}{1 - e^{-\tau_\nu}} d\nu \text{ cm}^{-2}, \quad (2)$$

where $Q(T_{ex})$ is the rotational partition function for a given excitation temperature, g_u is the rotational degeneracy of the upper level with energy E_u, A_{ul} is the Einstein A coefficient for the transition, k is the Boltzmann constant, h is the Planck constant, $J_\nu = (h\nu/k)/[\exp(h\nu/kT) - 1]$ is the Planck function in temperature units (K), and $\tau_\nu/(1 - e^{-\tau_\nu})$ is a correction factor for non-zero optical depth (see, e.g. Goldsmith & Langer 1999). This assumes that all transitions have the same T_{ex}. Physical parameters for the relevant molecules and transitions (frequency, rotational partition function, Einstein A coefficients, etc.) were obtained from the JPL Spectral Line Catalogue (Pickett et al. 1998) and the Leiden Atomic and Molecular Data base (LAMBDA; Schöier et al. 2005).

To compute the column density, we assume an excitation temperature $T_{ex} = 30$ K. We assume that the gas temperature is the same as the dust temperature derived from the far-IR spectral energy distribution (SED) that Roccatagliata et al. (2013) used to compute a temperature map of the entire Carina region. As discussed in Mangum & Shirley (2015), assuming a single temperature is often a poor assumption and we expect that to be true for the Mystic Mountains. However, adopting higher excitation temperatures ($T_{ex} \approx 40 - 80$ K) or a variable excitation temperature within this range changes the estimated column density by a factor of $\lesssim 2$. In the absence of a better temperature measurement, we adopt a single number in this study. Maps of the spatially resolved column density calculation for each of the CO isotopologues are shown in Appendix B and median column densities in each pillar are reported in Table 2.

3.3 Molecular gas mass of the Mystic Mountains

We estimate the mass of the Mystic Mountains complex from the optical-depth corrected spatially resolved 2D CO column density map using the equation

$$M_{gas} = \mu_g m(\text{H}_2) A \left[\frac{\text{H}_2}{\text{CO}}\right] \Sigma N(\text{CO}), \quad (3)$$

where $[\text{H}_2/\text{CO}] = 1.1 \times 10^4$ (Pineda et al. 2010) is the abundance of H_2 compared to CO, $\mu_g = 1.41$ is the mean molecular weight (Kauffmann et al. 2008), $m(H_2)$ is the mass of molecular hydrogen, and A is the area of each pixel in the map. We compute a mass of $\sim 36\,M_\odot$ for the entire Mystic Mountains complex. More recent measurements find $[\text{H}_2/\text{CO}] = 6000$ (Lacy et al. 2017) which reduce the estimated mass by a factor of 2.

3.4 Clumps, cores, and YSOs

3.4.1 C^{18}O clumps

We repeat the dendrogram analysis on the C^{18}O data to identify clumps using this higher density tracer. As for the CO analysis, we use the following thresholds: an intensity minimum value of 6σ to ensure that we are using only well-detected emission, a minimum intensity of 2σ to define a separate peak, and a minimum number of pixels equivalent to three beams. The leaves (local maxima) detected with this analysis are shown in Fig. 5.

We extract the emission of the CO isotopologues within each C^{18}O leaf (see Table 3) and plot the summed line profiles in Fig. 6. In general, the most optically thick line, CO (shown with a solid line),

Table 3. Physical properties of dendrogram leaves shown in Fig. 5.

Leaf	MM	RA (J2000)	Dec. (J2000)	v_{src} [km s^{-1}]	$<R>$ [pc]	Δv [km s^{-1}]	$\sigma_{turb;\,1D}$ [km s^{-1}]	M_{H_2} [$M_\odot$]	M_{vir} [$M_\odot$]	Stable?	Comment
L1	HH 1066 MM	10:44:05.4	−59:29:40	−8.4	0.02	1.3	0.53	4.9	4.1	N	
L2	MM1	10:44:05.4	−59:29:50	−7.1	0.03	1.5	0.64	48.7	9.0	N	^{13}CS
L3		10:44:05.2	−59:29:56	−7.0	0.02	1.3	0.52	5.6	4.5	N	
L4	MM2	10:44:02.9	−59:30:02	−7.5	0.02	0.93	0.37	5.9	1.9	N	
L5	MM3	10:43:59.7	−59:30:09	−7.0	0.02	1.1	0.43	4.5	2.6	N	
L6	MM4	10:44:01.1	−59:30:19	−8.0	0.02	1.1	0.45	15.7	2.6	N	DCN, ^{13}CS
L7	HH 902 MM	10:44:01.7	−59:30:27	−7.8	0.02	1.2	0.50	17.8	3.3	N	DCN, ∼2.7″ offset
L8	MM5	10:44:05.3	−59:30:20	−5.1	0.01	1.1	0.46	3.5	3.0	N	
L9		10:44:03.3	−59:30:45	−5.1	0.03	1.1	0.47	19.7	4.4	N	
L10	HH 901 MM	10:44:03.3	−59:30:60	−5.2	0.02	0.58	0.21	0.95	0.66	N	

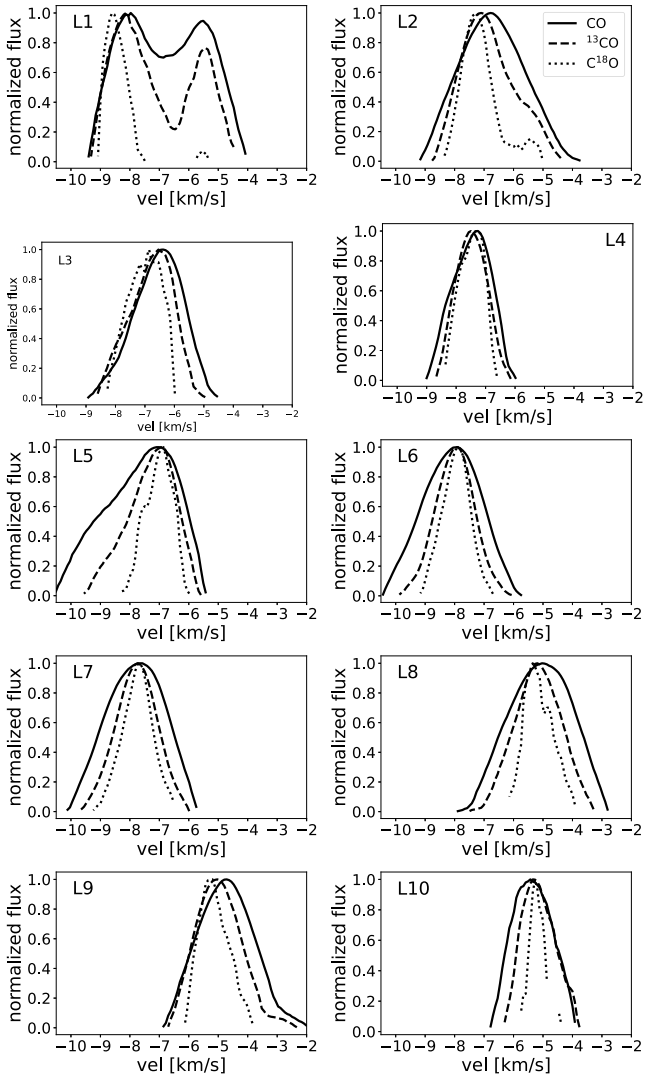

Figure 6. The summed intensity profile of each dendrogram leaf identified in the $C^{18}O$ data (see Fig. 5). Solid line is CO, dashed line is ^{13}CO and dotted line is $C^{18}O$.

has the broadest line profile. ^{13}CO (dashed line) and $C^{18}O$ (dotted line) are each narrower, with some $C^{18}O$ profiles showing evidence of multiple velocity peaks. The three leaves associated with jet-driving sources are L1 (HH 1066), L7 (HH 902), and L10 (HH 901). L1 shows clear evidence of two distinct velocity components within the beam separated by ~ -2.65 km s^{-1}. None of the three show evidence of red- and blue-shifted emission in the linewings that indicates an associated molecular outflow. These are likely washed out in the larger ACA beam as molecular outflows were detected in both HH 901 and HH 902 by Cortes-Rangel et al. (2020).

We use the median $C^{18}O$ line profile of each leaf to estimate its virial mass. We compute the virial mass using the following equation:

$$M_{vir} = \frac{3(5-2n)}{8(3-n)\ln(2)} \frac{(\Delta v^2)R}{G}, \quad (4)$$

where n is the exponent of the density profile ($\rho \propto r^{-n}$; we assume $n = 2$), Δv is the $C^{18}O$ linewidth (full width at half-maximum; FWHM), R is the mean leaf radius, and G is the gravitational constant. Further corrections to account for the non-spherical morphologies will change these values by <10 per cent (Bertoldi & McKee 1992). Virial masses, along with the linewidths, and 1D velocity dispersions for each leaf are reported in Table 3. We compare this to the molecular mass of each clump, computed as in Section 3.3 using $[H_2/C^{18}O] = [H_2/CO] \times [^{12}CO/C^{18}O] = 6.16 \times 10^6$ using data from Wilson & Rood (1994) and Pineda et al. (2010). The molecular mass of all clumps is higher than their virial mass, suggesting that they unstable to collapse, as noted in Table 3.

3.4.2 *Continuum sources*

Fig. 7 shows continuum emission detected with significance $\gtrsim 5\sigma$. This reveals nine point sources. We detect continuum from clumps near the origin of all three of the famous HH jets in the Mystic Mountains – HH 901 MM, HH 902 MM, and HH 1066 MM. Five other continuum peaks fall within the Mystic Mountains (MM1–MM5); three of these reside in the HH 902 pillar (MM2–4; see Fig. 7). The final point source, MM6, lies outside the Mystic Mountains complex so we do not discuss it further.

All mm continuum sources are associated with a $C^{18}O$ leaf, although not all $C^{18}O$ leaves have a continuum detection. Continuum and $C^{18}O$ emission are well-aligned spatially in all leaves but L7 at the head of the HH 902 pillar. Using a 2D Gaussian fit, we determine an offset of $2.7'' \pm 0.1''$ (0.03 pc) between the $C^{18}O$ and continuum peaks. The continuum peak is offset toward the western side of the pillar, in the same direction as the HH 902 YSO seen at higher resolution by Cortes-Rangel et al. (2020). A second continuum source detected to the north-east of the HH 902 YSO, HH 902 B, is not resolved with our larger beam.

Three additional continuum sources reside further north in the HH 902 pillar. A distinct peak in the continuum and $C^{18}O$ emission

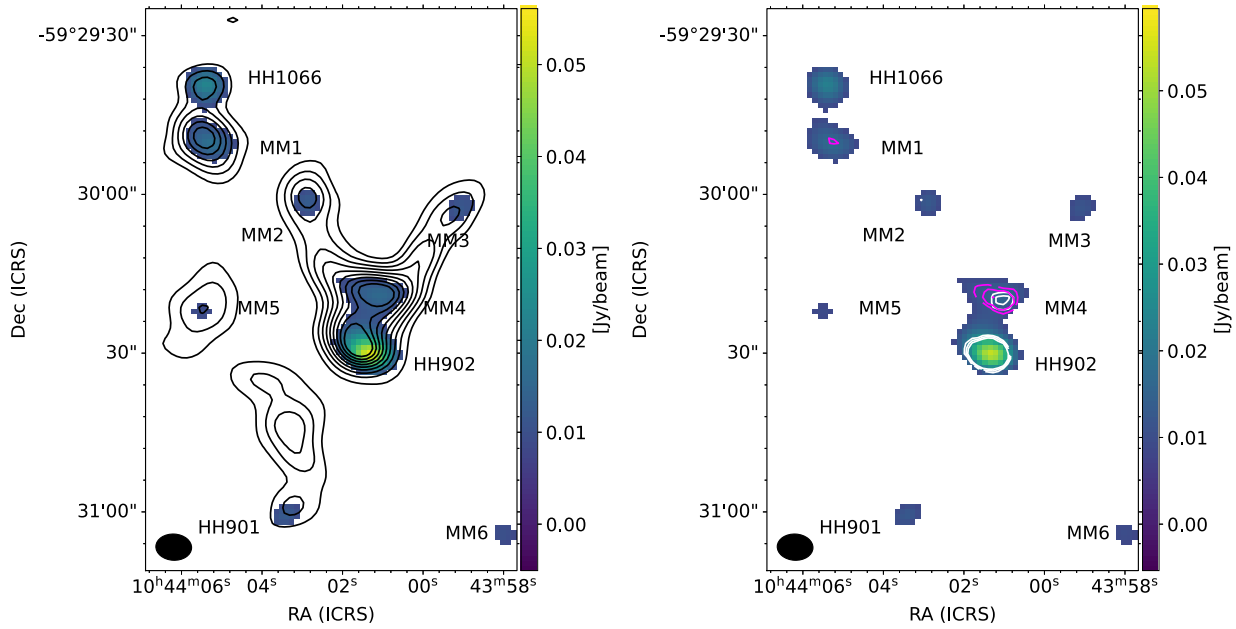

Figure 7. *Left:* colourscale of the aggregate continuum with $C^{18}O$ moment 0 contours from 10 to 100σ in steps of 10σ. *Right:* contours of the rarer molecules in our sample plotted on a colourscale of the continuum intensity. White contours show the DCN J=3–2 from 3 to 5σ and the magenta contours show ^{13}CS J=5–4 from 1 to 3σ.

traces MM4 immediately to the north of the HH 902 MM. A bridge of continuum emission connects the two sources. Two additional continuum sources lie further north in the wishbone-shaped HH 902 pillar. MM2 and MM3 coincide with $C^{18}O$ peaks at the east and west tips of the pillar.

To the east of the HH 902 pillar, there are three continuum sources in the HH 1066 pillar. At the top (northernmost point) of the HH 1066 pillar is HH 1066 MM. Due south lies MM1. Like its neighbour, continuum and $C^{18}O$ emission from MM1 appear to peak behind a cloud edge traced by bright Hα emission. Further south, MM5 coincides with a $C^{18}O$ peak at the head of the HH 1066 pillar, adjacent to the continuum emission from the HH 902 MM and MM4.

Finally, at the tip of the Mystic Mountains complex, the HH 901 pillar has one continuum source detected at the head of the pillar. The continuum source overlaps with a local peak in the $C^{18}O$ emission. However, the brightest $C^{18}O$ emission in the HH 901 pillar is seen at its center where there is no continuum detection.

We compute masses of the continuum sources as

$$M_d = S_\nu d^2 / B_\nu(T) \kappa_\nu. \quad (5)$$

We use a dust absorption coefficient $\kappa_\nu = 0.8\,\mathrm{cm^2\,g^{-1}}$ (Ossenkopf & Henning 1994) appropriate for 1.3 mm observations, and a temperature of T=30 K. We multiply the dust mass by a gas-to-dust ratio of 100 and report the total mass in Table 4. We have assumed a single temperature for all sources regardless of differences in their evolutionary stages (i.e. the presence of jets). Assuming a higher or lower temperature (15 or 45 K) changes the estimated mass by a factor of ~2. We refrain from a more detailed analysis given the low resolution of our data and evidence that multiple sources are unresolved in the beam (note that Cortes-Rangel et al. 2020, detect at least two point sources in the same region as our HH 902 MM). The flux and mass estimates of all continuum point sources are reported in Table 4.

Table 4. Properties of the continuum sources.

Source	RA (J2000)	Dec. (J2000)	225.9 GHz† [mJy]	Mass [$M_\odot$]
HH 1066 MM	10:44:05.421	−59:29:39.81	18.1	1.5
HH 902 MM	10:44:01.415	−59:30:29.84	65.9	5.3
HH 901 MM	10:44:03.463	−59:31:00.89	6.43	0.52
MM1	10:44:05.327	−59:29:50.65	13.3	1.1
MM2	10:44:02.939	−59:30:01.92	5.35	0.43
MM3	10:43:59.146	−59:30:02.95	6.25	0.51
MM4	10:44:01.255	−59:30:19.23	14.3	1.2
MM5	10:44:05.503	−59:30:22.43	4.76	0.39
MM6	10:43:58.069	−59:31:03.97	6.97	0.57

Note. †Aggregate continuum from the Band 6 observations.

3.4.3 *Candidate YSOs detected in other surveys*

Previous surveys at wavelengths <1.3 mm have also reported candidate YSOs in and around the Mystic Mountains. Three candidate YSOs from the Pan-Carina YSO Catalogue (PCYC; Povich et al. 2011) fall within the area of our ALMA map; these are shown on Fig. 5 as black diamonds. All three candidate YSOs have an ambiguous evolutionary classification. PCYC 429 was identified as the HH 1066 driving source by Reiter et al. (2016) and coincides with the continuum source HH 1066 MM and the $C^{18}O$ emission of L1. Immediately below HH 1066 MM, a second candidate YSO, PCYC 427, lies near the north-west boundary of L2, outside the continuum emission of MM1. PCYC 427 coincides with a point source visible in Hα images suggesting that this source lies in front of the cloud. Further west, a third candidate YSO, PCYC 399, is also visible in Hα images. This source falls well outside the lowest contour of CO emission from the HH 902 pillar and has no associated continuum emission, suggesting that it is also lies outside the cloud.

Ohlendorf et al. (2012) searched for YSOs driving the prominent jets in the Mystic Mountains and other dust pillars in Carina. They note a point-like source near HH 902 that is not detected at longer

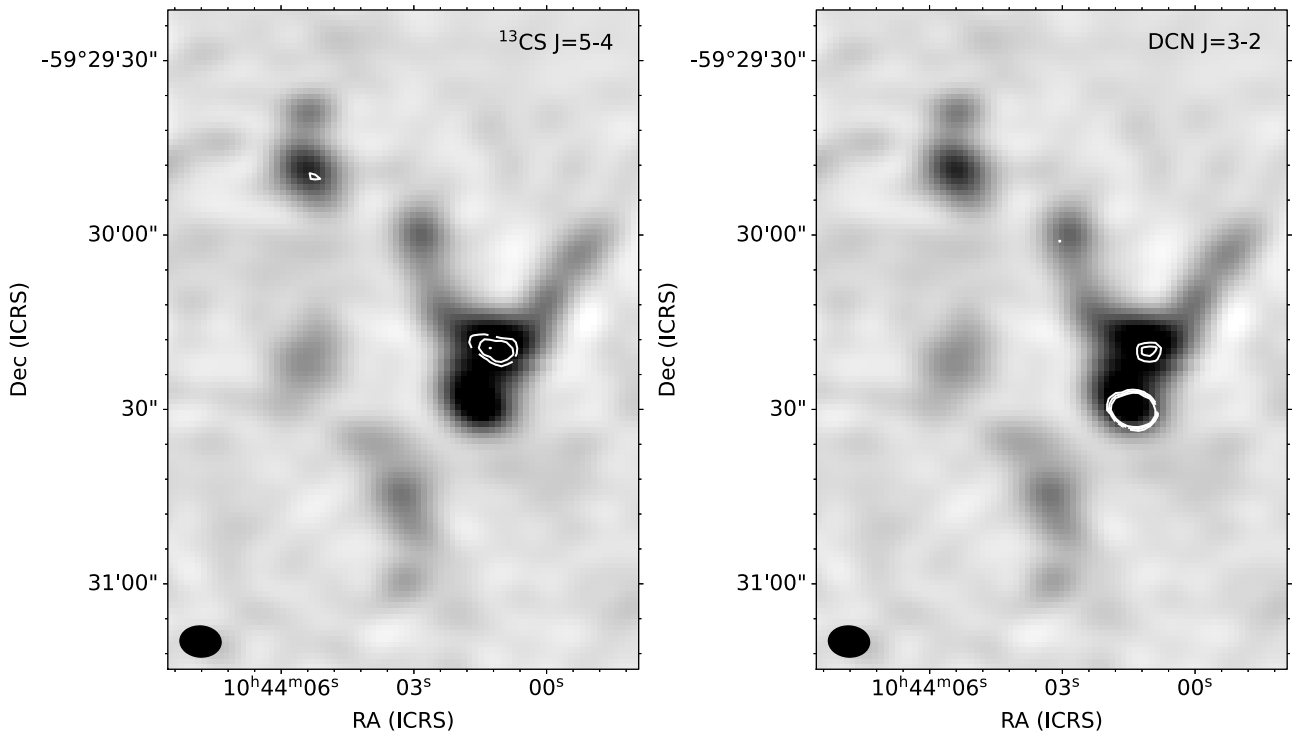

Figure 8. Moment 0 map of the $C^{18}O$ (greyscale) with contours of the ^{13}CS J=5–4 in steps of 1σ from 1 to 3σ (*left*) and DCN J=3–2 emission in steps of 1σ from 3 to 5σ (*right*).

Table 5. Summary of the rarer molecules. Columns are the species/transition, peak and median intensities, and median optically thin column density.

Source	I_{peak} [K km s^{-1}]	I_{median} [K km s^{-1}]	log(N)$_{peak}$	log(N)$_{median}$
		DCN J=3–2		
MM HH902	0.812	0.310	12.5	12.1
MM 4	0.298	0.116	12.1	11.7
		^{13}CS J=5–4		
MM 4	0.355	0.136	12.3	11.9
MM 1	0.121	0.076	11.8	11.6

(>8 μm) wavelengths; this is shown as a cyan square in Fig. 5. This source falls within HH 902 MM but is offset to the left, closer to the peak of the $C^{18}O$ emission. Coordinates reported by Ohlendorf et al. (2012) place the source ∼4″ away from the HH 902 YSO seen with ALMA by Cortes-Rangel et al. (2020). Together this suggests at least 3 YSOs unresolved in the HH 902 MM. Finally, no *Herschel* point sources were identified in the Mystic Mountains in the unbiased search by Gaczkowski et al. (2013).

3.5 Rarer species

Our observations included two rarer molecules, ^{13}CS J=5–4 and DCN J=3–2. ^{13}CS is a high-density tracer, typically seen in molecular envelopes and cavity walls (Tychoniec et al. 2021). DCN is most often observed in cold gas, where CO is frozen out of the enabling deuterium chemistry (Caselli & Ceccarelli 2012). Contour plots showing the emission peaks of both lines are presented in Fig. 8 and Table 5. The strongest ^{13}CS J=5–4 emission is associated with MM4. A second, weaker feature coincides with MM1.

DCN J=3–2 was serendipitously detected in a spectral window centered on SiO J=5–4; we do not detect SiO J=5–4 in any part of the mosaic. The brightest DCN peak is at the head of the HH 902 pillar, coincident with the HH 902 MM continuum source. Like the continuum emission, DCN is offset to the west of the $C^{18}O$ emission (see Fig. 7).

DCN emission coincident with the HH 902 MM presents a double-peaked velocity profile, shown in Fig. 9. The red peak is within 0.2 km s^{-1} of the velocity peak of the $C^{18}O$ emission from the same region. The second peak is blueshifted by ∼1 km s^{-1}. This velocity separation is not consistent with the frequency of any of the hyperfine components of DCN (using data from the Cologne Data base for Molecular Spectroscopy; CDMS; Müller et al. 2001, 2005). The flux of both peaks is remarkably similar, contrary to expectation for optically thin hyperfine emission. Finally, the velocity gradient is marginally resolved across the HH 902 MM (see Fig. 9). Cortes-Rangel et al. (2020) observed a similar velocity gradient in N_2D^+ J=3–2 (note that their observations have ∼20 × better spatial resolution). Both deuterated molecules show a velocity gradient that is oriented *opposite* to the velocity structure of the HH 902 molecular outflow – that is, redshifted DCN (N_2D^+) is seen on the same side of the YSO as the blueshifted limb of the outflow.

A second, fainter DCN peak coincides with MM4. The emission peaks of all three molecules – DCN, ^{13}CS, and $C^{18}O$ – coincide with continuum emission from MM4. Weak DCN emission extends from the position of MM2 along the edge of the pillar (see Fig. 2).

3.6 Velocity structure

Intensity-weighted velocity (moment 1) maps of the CO isotopologues are shown in Fig. 10. The most prominent feature is the velocity difference between the pillars of the Mystic Mountains.

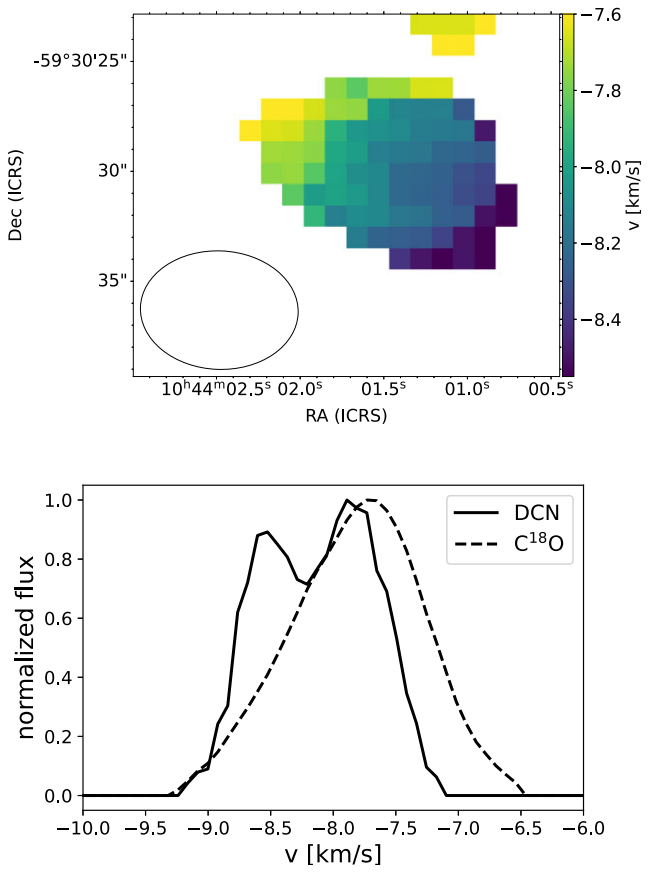

Figure 9. *Top:* moment 1 map of the DCN J=3–2 emission at the tip of the HH 902 pillar (see Fig. 8) that shows the velocity gradient across the marginally resolved source (the beam is shown in the lower left). *Bottom:* spectrum of the summed DCN J=3–2 emission compared to $C^{18}O$ spectrum from the same region.

Some velocity differences are also apparent along the north/south axis of the HH 1066 pillar and the wishbone-like extensions of the HH 902 pillar. $C^{18}O$ emission suggests that there are multiple clumps in the HH 1066 pillar with slightly different velocities. Higher resolution observations are required to determine if the inter-clump gas is at a markedly different velocity, as seen in Pillar 6 of Klaassen et al. (2020).

3.7 Non-thermal motions

To test whether photoionization contributes to the non-thermal motions in the pillars, we compare the average velocity dispersion to the incident ionizing photon flux. To probe a larger range of fluxes, we compare the Mystic Mountains to the dust pillars in Carina from Klaassen et al. (2020) because those observations use the same angular resolution and spectral setup as this work. As in Klaassen et al. (2020), we compute the average velocity dispersion from the moment 2 map. We consider the Mystic Mountains as a whole and each of the three pillars within it separately. To calculate the incident ionizing photon flux, we assume that the three main star clusters, Tr14, Tr15, and Tr16, dominate the external irradiation for all pillars in Carina. This provides a lower bound as we neglect the large number of O- and B-type stars located outside these clusters (see, e.g. Berlanas et al. 2023) and the effects of extinction. We use the ionizing photon luminosities from Smith (2006a) and compute the local flux using the projected distance between the pillars and the clusters.[2] The mean pillar velocity dispersion as a function of incident ionizing photon flux is shown in Fig. 11 (colour-coded by whether the pillars contain a jet seen at visual wavelengths, see discussion in Section 4.1).

Within the (large) uncertainties, the mean velocity dispersions are similar across nearly two orders of magnitude in incident ionizing radiation. This is counter to expectation if ionizing radiation drives turbulence in the gas. However, moment 2 maps do not isolate non-thermal motions from other factors that contribute to the linewidth. Bulk motions from large-scale processes like infall and rotation as well as the influence of outflows from protostars embedded in the pillars will all contribute to this single value. In addition, higher temperatures will increase the thermal contribution to the linewidth. However, to first order we would expect pillars subject to higher ionizing photon fluxes would also have warmer temperatures (see, e.g. the dust temperature maps from Roccatagliata et al. 2013; Rebolledo et al. 2016).

For the Mystic Mountains we separate thermal and turbulent motions as follows. We use the linewidth measured as the full width at half-maximum (Δv) to calculate the 1D velocity dispersion, $\sigma = \Delta v / 2\sqrt{2 \ln 2}$. To compute the thermal contribution, we use $\sigma_{\rm therm;1D} = \sqrt{2 k_B T / m_{\rm iso}}$, where $m_{\rm iso}$ is the mass of the CO isotopologue used and T=30 K is the temperature of the cold molecular gas. Subtracting the thermal component from the total velocity dispersion yields the 1D turbulent velocity dispersion, $\sigma_{\rm turb;1D} = \sqrt{\sigma_{\rm tot}^2 - \sigma_{\rm therm}^2}$. Finally, we convert the 1D estimate to 3D as $\sigma_{\rm turb} = \sqrt{3}\sigma_{1D}$. The 3D turbulent velocity dispersion computed for each CO isotopologue is shown in Fig. 12.

Velocity dispersions are higher in CO than in ^{13}CO and $C^{18}O$. The highest values for the turbulent velocity dispersion are observed where the pillars overlap, almost certainly reflecting the influence of multiple velocity components along the line of sight. Other regions with high values of the velocity dispersion fall behind ionization fronts traced by Hα (see Fig. 13).

The HH 902 pillar is well resolved with our $\sim 6''$ beam and overlaps only minimally with the other pillars in the Mystic Mountains. Qualitatively, the velocity dispersion is higher where the Hα emission is higher. Velocity dispersions are larger along the western edge of the pillar and modest peaks appear behind the two Hα ridges at the head of the pillar. Peaks in the velocity dispersion do not coincide with the location of the continuum sources.

When estimating $\sigma_{\rm therm;\,3D}$, we assumed a single temperature of T=30 K for the entire Mystic Mountains. Gas temperatures are likely higher in the most heavily irradiated parts of the Mystic Mountains. Assuming a higher temperature, T=50 K, yields a larger thermal contribution $\sigma_{\rm therm;\,1D} = 0.59\,{\rm km\,s^{-1}}$ which is roughly equivalent to the average velocity dispersion of the Mystic Mountains (as estimated from the moment 2 map).

In addition to temperature uncertainties, the lack of correlation between velocity dispersion and incident ionizing photon flux may result from one of the following possibilities: (1) turbulence is enhanced only near irradiated cloud surfaces in layers too thin to be resolved with our $\sim 6''$ beam; (2) different pillars have a different level of embedded star formation that contributes unequally to the observed linewidth (i.e. via outflows) but is unresolved in our beam (and star formation activity itself does not vary as a function of

[2]The nearest cluster in projection does not always dominate the ionization. For example, Pillar 20 lies alongside Tr15 but points toward Tr16, suggesting that it has had a stronger influence.

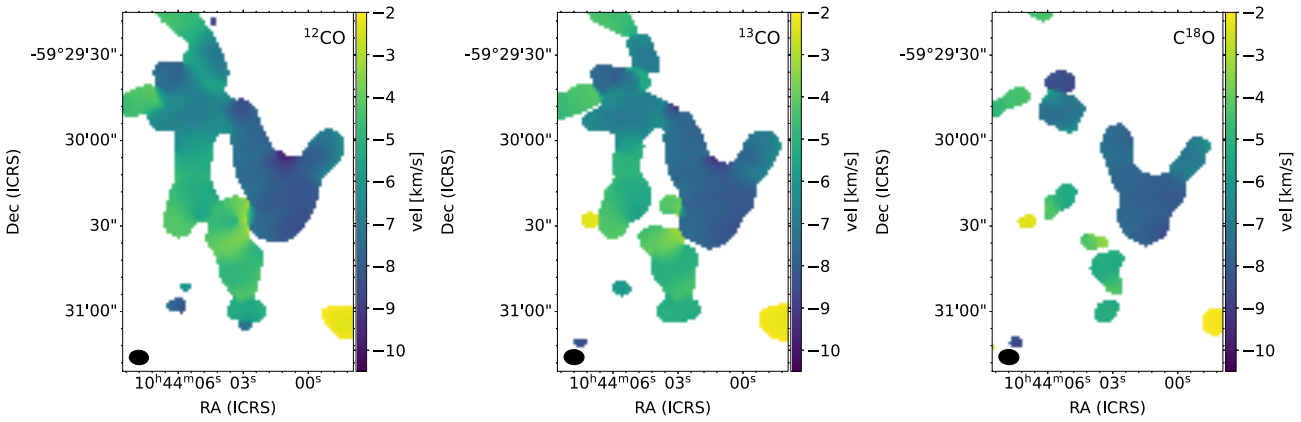

Figure 10. Intensity-weighted velocity (moment 1) maps of the CO isotopologues.

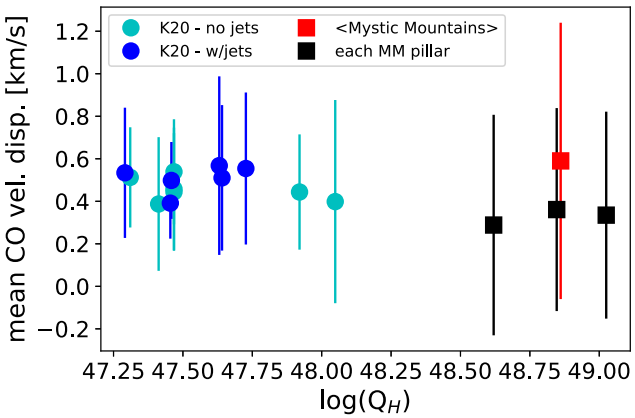

Figure 11. Mean CO velocity dispersion compared to the estimated incident ionizing photon luminosity for the three pillars in the Mystic Mountains (black squares) and the average of the Mystic Mountains (red square). These are compared to other pillars in Carina observed with the same resolution and spectral setup from Klaassen et al. (2020) with (blue) and without (cyan) one or more prominent jets seen at visual wavelengths. All three pillars in the Mystic Mountains complex have at least one jet.

incident ionizing flux); or (3) that ionizing radiation does not drive turbulence.

However, the velocity dispersion may not be best discriminant of the impact of ionizing radiation on the gas. External radiation may drive non-thermal motions through compressive shocks but shock energy will quickly dissipate and the velocity signature may not be long-lived. Compressive motions will also reshape the density of the gas, leaving behind local regions of higher density. We consider this signature of compressive turbulence in the next section.

3.8 Isolating turbulent motions

Menon et al. (2021) used the data of Klaassen et al. (2020) to measure the turbulence in a few well-resolved pillars. They reconstruct the dominant turbulence driving mode from the column density and intensity-weighted velocity maps (Federrath et al. 2010, 2016). In this section, we repeat this analysis for the Mystic Mountains complex for a highly irradiated comparison.

3.8.1 2D density structure

To compute the density probability distribution function (PDF), we use the column density of the optically thin ^{13}CO as a proxy for the H_2 along the line of sight, N, substituting the C^{18}O in places where the ^{13}CO is optically thick. We compute σ_η, the dispersion of the natural logarithm of the column density scaled by its mean ($\eta = \log(N/N_0)$) by fitting a Hopkins (2013) intermittency density PDF model to the volume-weighted PDF of η. This has the form

$$p_{\rm HK}(\eta)d\eta = I_1(\sqrt{2\lambda\omega(\eta)}\exp\left[-(\lambda+\omega(\eta))\right]\sqrt{\frac{\lambda}{\theta^2\omega(\eta)}}d\eta, \quad (6)$$

where

$$\lambda = \frac{\sigma_\eta^2}{2\theta^2}, \quad (7)$$

and

$$\omega(\eta) = \frac{\lambda}{(1+\theta)} - \frac{\eta}{\theta} \ (\omega \geq 0), \quad (8)$$

and θ is the intermittency parameter. The values of σ_η and θ derived from the fit are used to compute σ_{N/N_0}, the linear dispersion, as

$$\sigma_{N/N_0} = \sqrt{\exp\left(\frac{\sigma_\eta^2}{(1+3\theta+2\theta^2)}\right) - 1}, \quad (9)$$

using an expression from Hopkins (2013).

3.8.2 Conversion from 2D to 3D density structure

We estimate the 3D density dispersion from the 2D column density dispersion using the method of Brunt, Federrath & Price (2010). The 3D density power spectrum, $P_{3D}(k)$, of the variable $\rho/\rho_0 - 1$ is reconstructed from the 2D column density power spectrum, $P_{2D}(k)$, of the variable $N/N_0 - 1$; k is the wavenumber. This is converted to the 3D power spectrum as $P_{3D}(k) = 2kP_{2D}(k)$. The ratio $\mathcal{R}^{1/2}$ of the 2D and 3D dispersions is defined as

$$\mathcal{R}^{1/2} = \frac{\sigma_{N/N_0}}{\sigma_{\rho/\rho_0}} = \frac{\sum_k P_{2D}(k)}{\sum_k P_{3D}(k)}, \quad (10)$$

where we have mirrored the column density to provide a periodic data set (Ossenkopf, Krips & Stutzki 2008).

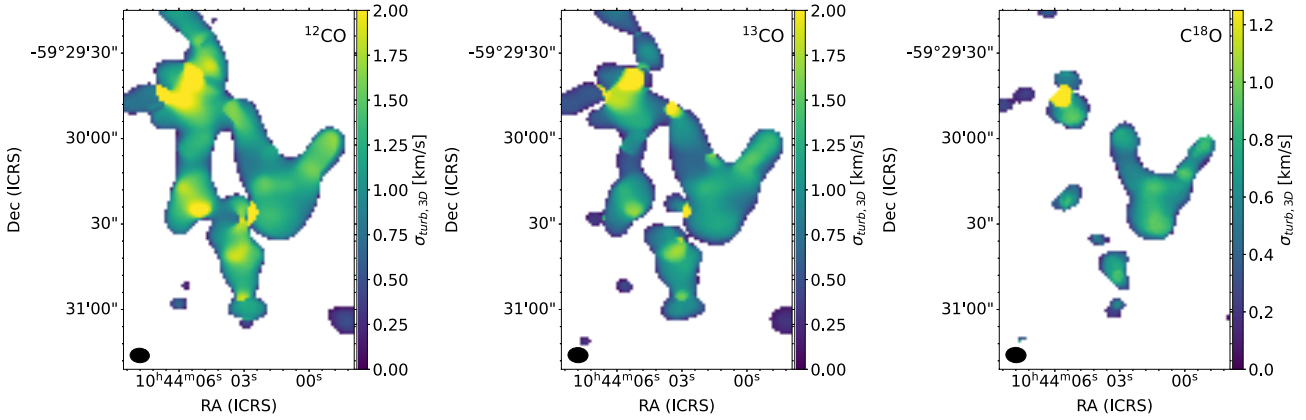

Figure 12. The 3D turbulent velocity dispersion computed assuming a single gas temperature of $T = 30$ K.

3.8.3 *Isolating turbulent motions*

We fit a plane to the intensity-weighted velocity map (the first moment map) to remove bulk motions and isolate turbulent motions in the pillars. For purely turbulent motion, we expect the line-of-sight motions to trace a Gaussian PDF. We fit a Gaussian to the line-of-sight velocity PDF to derive the 1D velocity dispersion, $\sigma_{v,\,1D}$. We convert this to the 3D velocity dispersion as $\sigma_{v,\,3D} = 3^{1/2}\sigma_{v,\,1D}$, implicitly assuming isotropy.

From this, we compute the Mach number, $\mathcal{M} = \sigma_{v,3D}/c_s$, which is the ratio of the 3D velocity dispersion and the sound speed, $c_s \sim 0.3\,\mathrm{km\,s^{-1}}$ for our assumed temperature of 30 K. Finally, we compute b, the turbulence driving parameter as $b = \sigma_{\rho/\rho_0}/\mathcal{M}$. The value of b is used to determine the type of turbulence: $b \sim 0.33$ is purely solenoidal; $b \sim 1.0$ is purely compressive; and $b \sim 0.4$ is a combination of both.

Values of each of the derived parameters and their 1σ uncertainties are listed in Table 6. PDFs of the column density and velocities for the Mystic Mountains are shown in Fig. 14. We focus our comparison on the Mystic Mountains as a whole because the individual pillars are significantly smaller, with only a few beams covering their major and minor axes. Results of this analysis for each individual pillar are shown in Appendix C but we do not discuss them further here as the individual pillars are inadequately resolved for this analysis (similar to Pillar 44 in Menon et al. 2021; see also Sharda et al. 2018).

3.8.4 *Comparing the Mystic Mountains to other pillars in Carina*

Within the Mystic Mountains, it is clear that there are multiple velocity components; these roughly correspond to the systemic velocity of each pillar (see Fig. 14 and Table 2). Subtracting a linear function (a plane) reduces the peakiness of the velocity distribution, but the velocity dispersion remains large even after gradient subtraction, nearly a factor of two higher than the values found by Menon et al. (2021) for other pillars in Carina. As a result, the Mach number ($\mathcal{M} = \sigma_{v,3D}/c_s$) is also a factor of 2 higher. The resulting turbulence driving parameter b is within the range of compressively dominated turbulence ($0.4 - 1.0$) but somewhat lower than the values ($0.8 - 1.7$) found by Menon et al. (2021).

4 DISCUSSION

Recent numerical work suggests that ionizing radiation may drive turbulence in cold molecular gas via the rocket effect (e.g. Gritschneder et al. 2009; Boneberg et al. 2015; Dale 2017; Menon et al. 2020). Photoevaporation drives a flow of free electrons from ionized cloud surfaces. Momentum is conserved, so this flow also drives a shock into the cloud, compressing the gas, and perhaps injecting turbulence.

In this picture, highly irradiated pillars like the Mystic Mountains should show a high level of turbulent velocity dispersion in the gas. The Mystic Mountains cloud complex lies in the heart of the Carina Nebula where copious ionizing photons from Tr14 ($Q_H \sim 10^{50}\,\mathrm{s^{-1}}$, see Smith 2006a) illuminate and sculpt its mountainous morphology. The incident ionizing photon flux illuminating the Mystic Mountains is an order of magnitude higher than that illuminating other pillars in Carina with similar observations (see Fig. 11 and Klaassen et al. 2020).

A clear correlation between the incident ionizing radiation and electron density in ionization fronts has been observed in dust pillars in Carina (McLeod et al. 2016). We do not find a similarly straightforward relationship between the cold molecular gas and incident radiation. Despite the higher ionizing flux illuminating the Mystic Mountains, the average velocity dispersion (derived from the moment 2 map) is comparable to other pillars in Carina (see Fig. 11). At $b = 0.55$, the turbulence driving parameter is consistent with compressive turbulence but is below the range found by Menon et al. (2021).

For all of the pillars in Carina that have been observed with the ACA alone, it is unclear what role unresolved star formation activity plays in the observed kinematics. In the Mystic Mountains, we detect 8 continuum sources (see Section 3.4.2) and 10 C^{18}O clumps (see Section 3.4). The pillars in the Klaassen et al. (2020) also display a wide range of star-formation activity from the relatively quiescent Pillar 22 which has only two C^{18}O cores to the actively star-forming Pillar 6 with evidence for >4 separate YSOs. Protostars and their (unresolved) outflows can contribute to internal velocity dispersion (e.g. Larson et al. 2015) and may provide a local source of turbulence. Quantifying this is difficult, however, as we do not detect the known outflows in the Mystic Mountains or any other molecular outflows, likely due to the modest resolution of our data (at 2.3 kpc, our $\sim 6''$ beam corresponds to $\sim$0.07 pc). The physical properties of the famous jets in the Mystic Mountains (see Fig. 1) are well measured (Reiter & Smith 2013, 2014; Cortes-Rangel et al. 2020) but these largely propagate outside the cloud.

Higher angular resolution observations are required to detect and remove the influence of embedded outflows as well as analyse the individual pillars of the Mystic Mountains independently. Existing data covers a small region at the head of the HH 901 and HH 902 pillars (Cortes-Rangel et al. 2020); extending this to a larger portion

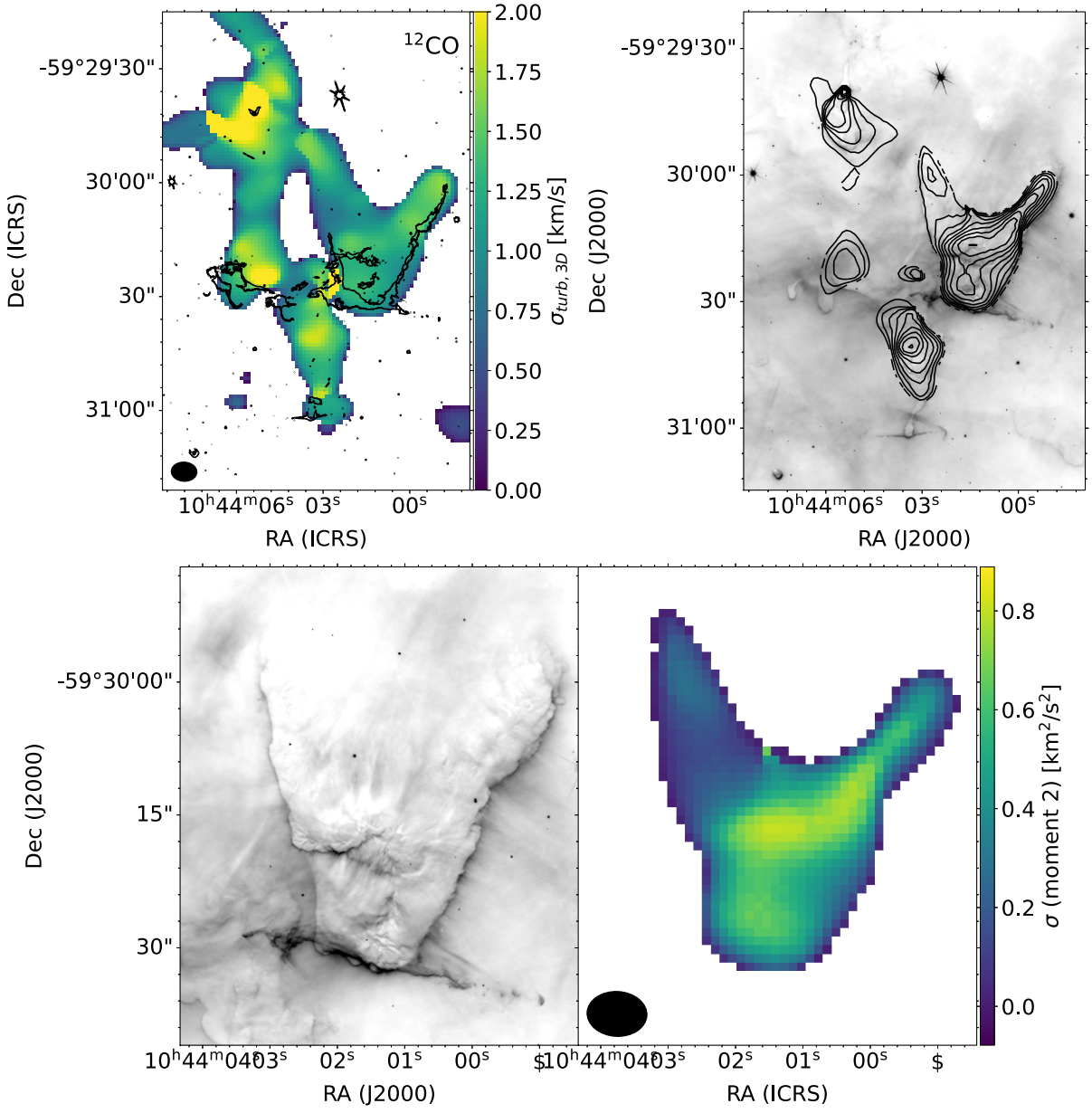

Figure 13. *Top Left:* map of the CO turbulent velocity dispersion with H α contours overplotted in black. *Top Right:* contours from the CO moment 2 map plotted on a greyscale of the H α image from *HST*. Many peaks in the velocity dispersion correspond to regions where the pillars appear to overlap. The one exception is HH 902 which we zoom in on in the bottom two panels. *Bottom:* a zoomed-in view of the HH 902 pillar showing the *HST* H α image alongside the CO moment 2 map. Both the H α intensity and the CO velocity dispersion are higher along the western side of the HH 902 pillar.

of the Mystic Mountains would be interesting to do in the future. For now, we compare the results of the Mystic Mountains and the Klaassen et al. (2020) pillars to higher resolution observations of other portions of the Carina region.

4.1 Comparison to other regions in Carina

A few other studies in the Carina region have quantified the impact of ionizing feedback on star-forming gas. Rebolledo et al. (2020) compared two clouds in the Carina region that are subject to very different ionizing radiation fields: the 'North Cloud' which is located near the center of Carina where it is heavily irradiated by Tr14 and the 'South Pillars' regions which is located in the outskirts of Carina where it is subject to much less intense radiation. The two regions are separated from the central clusters, Tr14 and Tr16, by ∼2.5 pc and ∼30 pc, respectively, and thus experience an order of magnitude difference in their radiative environment. With Band 3 observations targeting the dense gas tracers HCN and HCO$^+$ with a resolution of $2.8'' \times 1.8''$, Rebolledo et al. (2020) find evidence for more turbulence in the heavily irradiated North Cloud. The North Cloud also has fewer cores than the South Pillars region. However, the cores that have formed in the North Cloud are higher in mass than the more numerous cores found in the South Pillars cloud, consistent with turbulent fragmentation.

Hartigan et al. (2022) recently published observations of the 'Western Wall,' a region in the center of Carina that overlaps

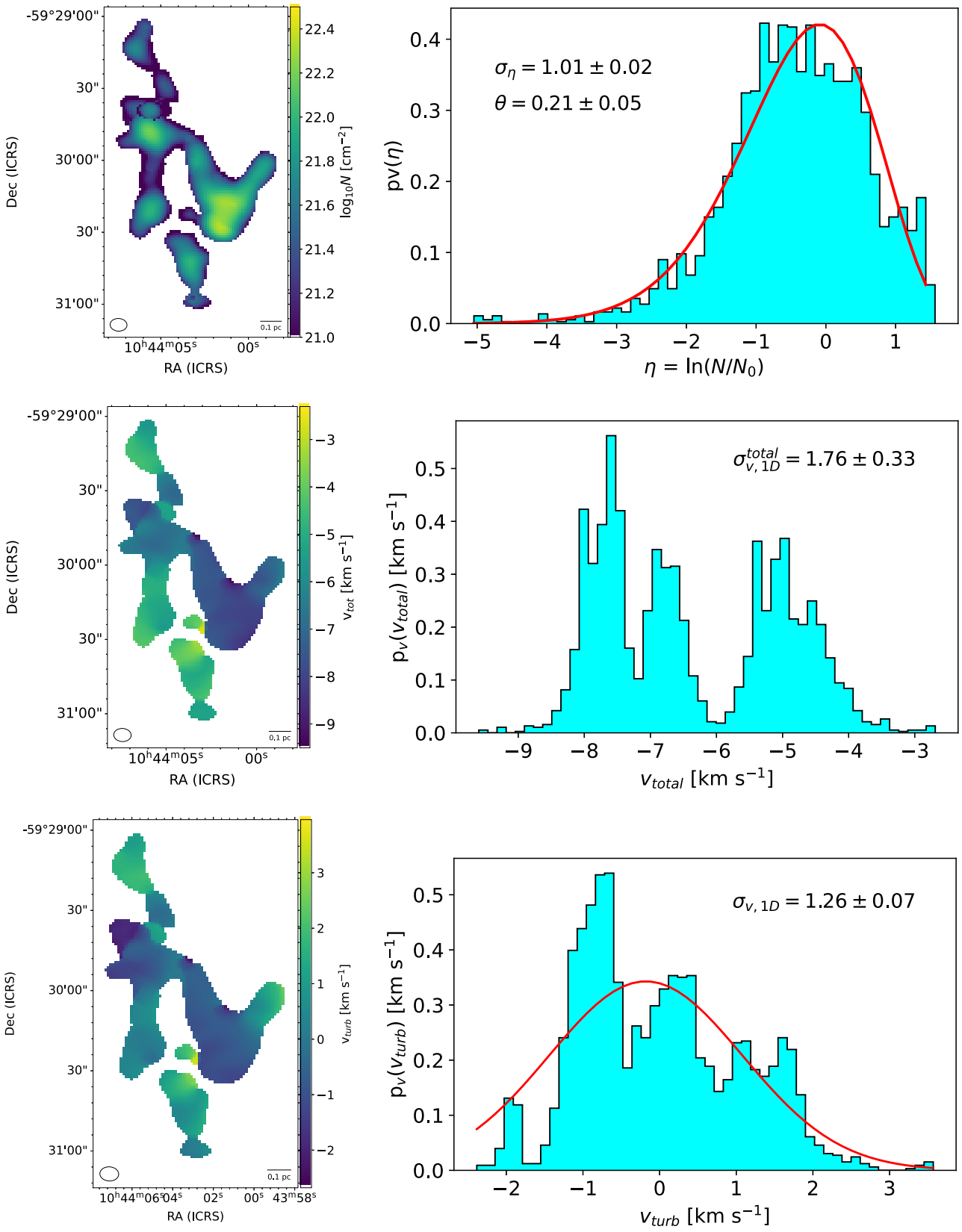

Figure 14. *Top:* left panel shows the H_2 column density derived from the optically thin ^{13}CO and $C^{18}O$ (see Section 3.7). Right panel shows the fit to the column density PDF, as in Menon et al. (2021). *Middle:* image of the intensity-weighted velocity map prior to gradient subtraction (left) and histogram of its distribution (right). *Bottom:* velocity map (left) and histogram (right) after gradient subtraction.

Table 6. Turbulence parameters for the Mystic Mountains as a whole, as in Menon et al. (2021).

Pillar	MM
A [pc^2]	0.32 ± 0.03
N_0 [10^{21} cm^{-2}]	$3.01^{+5.3}_{-1.9}$
M [M$_\odot$]	33.7 ± 5.7
n [10^3 cm^{-3}]	2.33 ± 1.3
$\sigma_{v,3D}^{M2}$ [km s^{-1}]	0.34 ± 0.30
α_{vir}	26.7 ± 15
t_{ff}/t_{turb}	2.22 ± 0.62
σ_η	1.01 ± 0.02
σ_{N/N_0}	0.56 ± 0.02
$\mathcal{R}^{1/2}$	0.14 ± 0.01
σ_{ρ/ρ_0}	4.02 ± 0.37
$\sigma_{v,1D}^{\rm total}$ [km s^{-1}]	1.76 ± 0.33
$\sigma_{v,1D}$ [km s^{-1}]	1.26 ± 0.07
$\sigma_{v,3D}$ [km s^{-1}]	2.19 ± 0.13
$\mathcal{M}$	7.29 ± 0.43
b	0.55 ± 0.05

with the North Cloud from Rebolledo et al. (2020). These higher resolution observations (synthesized beamsize $\sim 1''$) in Band 6 target CO and its isotopologues. Hartigan et al. (2022) conclude that the influence of feedback is modest with no signs of triggered star formation and no prominent dust pillars. Gas densities appear higher immediately behind the ionization front but cores appear starless, and there is no evidence for grain growth. A follow-up analysis of the Hartigan et al. (2022) observations from Downes, Hartigan & Isella (2023) determined that turbulence is driven at large scales, but not necessarily by irradiation from nearby high-mass stars.

This conclusions stands in contrast to Menon et al. (2021) who argue that pre-dominantly compressive modes of turbulence may have triggered star formation in the pillars. However, Downes et al. (2023) argue that their result is not in tension with Menon et al. (2021). Unlike the Western Wall, the pillars have been sculpted by radiation. Pillars may self-shadow, allowing compressive motions to lead to their development, altering their internal kinematics.

In the simulations of Dale et al. (2012), prominent pillars form in clouds with more diffuse gas and those with smoother density fields. Above a certain density ($\gtrsim$100 cm^{-3}), ionization is dynamically ineffective, especially in more turbulent regions. On the smaller scales of the pointed observations presented in this paper and those in Klaassen et al. (2020), Rebolledo et al. (2020), and Hartigan et al. (2022), differences in the local initial conditions may be responsible for the morphological differences observed at present. In this case, ionizing radiation carved more diffuse gas into dust pillars, perhaps triggering star formation (Brooks et al. 2002; Rathborne et al. 2004; Smith et al. 2010b; Ohlendorf et al. 2012). Meanwhile, the higher density Western Wall/North Cloud began as and remained a higher density region (see, e.g. fig. 1 in Rebolledo et al. 2020), less vulnerable to compression. Local density variations may also help explain why there is a dust pillar $\sim 1'$ ($\sim$0.7 pc) to the north-east of the Western Wall (see Smith et al. 2010a).

This picture is in line with the simulations of Tremblin et al. (2012a, b) who find that pillar formation depends strongly on shock curvature. Pre-existing overdensities help curve the shock driven by the ionization front. Pillars form when the curved shock collapses in on itself. Pillars formed in this way will naturally have a high-density core at their tips in much the same way that desert buttes have high-density caprock at their apices.

While differences in the initial density may help explain the absence of pillars in the Western Wall, the low level of star formation activity remains a challenge. High initial densities in the Western Wall suggest that star formation would happen sooner than in the feedback-carved pillars. But this is not what is observed. Hartigan et al. (2022) find that the cores in the Western Wall are starless. Rebolledo et al. (2020) argue that the higher level of turbulence may have made the Western Wall more resilient to fragmentation as there are fewer but higher mass cores compared to their more quiescent South Pillars region. In contrast, several pillars show evidence for star formation in the form of their prominent jets.

Turbulence rapidly decays and must be constantly resupplied to maintain observed levels. Rebolledo et al. (2020) attribute the higher turbulence in the North Cloud/Western Wall to the impact of external irradiation. Downes et al. (2023) also find evidence that turbulence is driven on large scales, but they do not attribute this to ionization. Resolving this tension requires a more homogeneous data set that covers the large (pc) scales where turbulence is driven while resolving the 0.02 – 0.03 pc scales that Downes et al. (2023) find are also dynamically important.

5 CONCLUSIONS

In this paper, we present maps of the CO, ^{13}CO, and C^{18}O emission from the Mystic Mountains, a large cloud complex with multiple dust pillars located in the heart of the Carina Nebula. A dendrogram analysis reveals a coherent, connected structure with three individual pillars. We detect eight continuum cores within the Mystic Mountains. Most continuum cores are associated with a C^{18}O clump, but not all C^{18}O clumps have a continuum counterpart. The rarer isotopologues DCN J=3–2 and ^{13}CS J=5–4 are detected in two clumps located in the region with the highest column density.

The Mystic Mountains region experiences an order of magnitude higher ionizing flux from the nearby star clusters than the flux incident on other dust pillars in Carina observed with similar tracers and angular resolution. However, bulk pillar properties like the average velocity dispersion derived from moment 2 maps are similar for all pillars, regardless of their irradiation.

A more detailed analysis to isolate turbulent motions reveals a turbulent driving parameter, $b = 0.55$, consistent with compressive turbulence dominating in the Mystic Mountains. The derived b is within the range of values found by Menon et al. (2021) for the pillars from Klaassen et al. (2020). The derived Mach number for the Mystic Mountains is a factor of 2 higher than that found for other pillars in the Carina region, either reflecting a stronger shock from the more intense UV field, or, more likely, is artificially inflated by the broad velocity distribution of the Mystic Mountains.

The similarity of pillar properties across a range of incident ionizing fluxes contrasts with studies of other irradiated clouds in the Carina Nebula. Rebolledo et al. (2020) compared two regions with an order of magnitude difference in the incident radiation and find evidence for more turbulence and fewer (but higher mass) cores in the more heavily irradiated cloud. From a different analysis and data set of the same region presented by Rebolledo et al. (2020), Downes et al. (2023) argue that differences between the pillar results and the cloud results are not inconsistent because pillar kinematics may reflect dynamical compression. We argue that this may be true if the different morphologies observed today result from different initial densities that aided or prevented UV irradiation from compressing the local cloud into a pillar. Pre-existing overdensities may also explain the observed difference in star-forming activity. Cores in the

Western Wall/North Cloud appear starless whereas a fraction of the cores in the Mystic Mountains and other pillars drive prominent jets, signifying a more advanced evolutionary stage (i.e. HH 901 and HH 902 in the Mystic Mountains; see Cortes-Rangel et al. 2020).

Future work probing a broader range of environments with the angular resolution to probe both the large scales of turbulence driving and the small scales where its consequences are most evident will help resolve this tension.

ACKNOWLEDGEMENTS

We would like to thank the referee, Neal Evans, for a prompt and thoughtful report that improved the manuscript. We would like to thank Shyam Menon for a careful reading of the manuscript and thoughtful feedback. MR was partially supported by an ESO fellowship. DI was funded by the European Research Council (ERC) via the ERC Synergy Grant ECOGAL (grant number 855130). This paper makes use of the following ALMA data: ADS/JAO.ALMA#2018.1.01001.S. ALMA is a partnership of ESO (representing its member states), NSF (USA) and NINS (Japan), together with NRC (Canada) and NSC and ASIAA (Taiwan) and KASI (Republic of Korea), in cooperation with the Republic of Chile. The Joint ALMA Observatory is operated by ESO, AUI/NRAO, and NAOJ. The National Radio Astronomy Observatory is a facility of the National Science Foundation operated under cooperative agreement by Associated Universities, Inc. This work uses observations made with the NASA/ESA *HST*, obtained from the Data Archive at the Space Telescope Science Institute, which is operated by the Association of Universities for Research in Astronomy, Inc., under NASA contract number NAS 5–26555. The HST observations are associated with GO-12050. This research made use of Astropy,[5] a community developed core Python package for Astronomy (Astropy Collaboration et al. 2013; Price-Whelan et al. 2018). This research made use of APLPY, an open-source plotting package for Python (Robitaille & Bressert 2012). This research made use of the following software packages: astrodendro, a Python package to compute dendrograms of Astronomical data (http://www.dendrograms.org/); SCIMES, a Python package to find relevant structures into dendrograms of molecular gas emission using the spectral clustering approach (Colombo et al. 2015); and TurbuStat, a Python package to compute 14 turbulence-based statistics described in the astronomical literature (Koch et al. 2017, 2019).

6 DATA AVAILABILITY

The ALMA data used in this study are publicly available from the ALMA archive[3] under the programme ID number ADS/JAO.ALMA#2018.1.01001.S. Data from *HST* are publicly available via the MAST archive.[4]

REFERENCES

Astropy Collaboration et al., 2013, A&A, 558, 33
Berlanas S. R., et al., 2023, A&A, 671, 20
Bertoldi F., 1989, ApJ, 346, L735
Bertoldi F., McKee C. F., 1992, ApJ, 395, L140
Boneberg D. M., Dale J. E., Girichidis P., Ercolano B., 2015, MNRAS, 447, 1341
Brooks K. J., Rathborne J. M., Burton M. G., Cox P., 2002, in Crowther P., ed., ASP Conf. Ser. Vol. 267, Hot Star Workshop III: The Earliest Phases of Massive Star Birth. Astron. Soc. Pac., San Francisco, p. 353
Brunt C. M., Federrath C., Price D. J., 2010, MNRAS, 403, 1507
Caselli P., Ceccarelli C., 2012, A&A Rev., 20, 56
Chevance M., et al., 2022, MNRAS, 509, 272
Choi M., Evans N. J. II, Jaffe D. T., 1993, ApJ, 417, L624
Colombo D., Rosolowsky E., Ginsburg A., Duarte-Cabral A., Hughes A., 2015, MNRAS, 454, 2067
Cortes-Rangel G., Zapata L. A., Toalá J. A., Ho P. T. P., Takahashi S., Mesa-Delgado A., Masqué J. M., 2020, AJ, 159, 62
Dale J. E., 2017, MNRAS, 467, 1067
Dale J. E., Ercolano B., Bonnell I. A., 2012, MNRAS, 424, 377
Downes T. P., Hartigan P., Isella A., 2023, MNRAS, 519, 5427
Elmegreen B. G., Lada C. J., 1977, ApJ, 214, L725
Federrath C., Roman-Duval J., Klessen R. S., Schmidt W., Mac Low M. M., 2010, A&A, 512, 81
Federrath C., et al., 2016, ApJ, 832, L143
Gaczkowski B., Preibisch T., Ratzka T., Roccatagliata V., Ohlendorf H., Zinnecker H., 2013, A&A, 549, 67
Goldsmith P. F., Langer W. D., 1999, ApJ, 517, L209
Goodman A. A., Pineda J. E., Schnee S. L., 2009, ApJ, 692, L91
Göppl C., Preibisch T., 2022, A&A, 660, 11
Gritschneder M., Naab T., Walch S., Burkert A., Heitsch F., 2009, ApJ, 694, L26
Gritschneder M., Burkert A., Naab T., Walch S., 2010, ApJ, 723, L971
Hartigan P., Reiter M., Smith N., Bally J., 2015, AJ, 149, 101
Hartigan P., Hummel M., Isella A., Downes T., 2022, AJ, 164, 257
Hester J. J., et al., 1996, AJ, 111, 2349
Hopkins P. F., 2013, MNRAS, 430, 1880
Jacob A. M., Menten K. M., Wiesemeyer H., Güsten R., Wyrowski F., Klein B., 2020, A&A, 640, 125
Kauffmann J., Bertoldi F., Bourke T. L., Evans N. J. II, Lee C. W., 2008, A&A, 487, 993
Klaassen P. D., Mottram J. C., Dale J. E., Juhasz A., 2014, MNRAS, 441, 656
Klaassen P. D., Reiter M. R., McLeod A. F., Mottram J. C., Dale J. E., Gritschneder M., 2020, MNRAS, 491, 178
Koch E. W., Ward C. G., Offner S., Loeppky J. L., Rosolowsky E. W., 2017, MNRAS, 471, 1506
Koch E. W., Rosolowsky E. W., Boyden R. D., Burkhart B., Ginsburg A., Loeppky J. L., Offner S. S. R., 2019, AJ, 158, 1
Kruijssen J. M. D., et al., 2019, Nature, 569, 519
Lacy J. H., Sneden C., Kim H., Jaffe D. T., 2017, ApJ, 838, L66
Larson R. L., Evans N. J. II, Green J. D., Yang Y.-L., 2015, ApJ, 806, L70
Mangum J. G., Shirley Y. L., 2015, PASP, 127, 266
Matzner C. D., 2002, ApJ, 566, L302
McLeod A. F., et al., 2016, MNRAS, 462, 3537
McLeod A. F., et al., 2021, MNRAS, 508, 5425
McMullin J. P., Waters B., Schiebel D., Young W., Golap K., 2007, in Shaw R. A., Hill F., Bell D. J., eds., ASP Conf. Ser. Vol. 376, Astronomical Data Analysis Software and Systems XVI, San Francisco, p. 127
Menon S. H., Federrath C., Kuiper R., 2020, MNRAS, 493, 4643
Menon S. H., Federrath C., Klaassen P., Kuiper R., Reiter M., 2021, MNRAS, 500, 1721
Mesa-Delgado A., Zapata L., Henney W. J., Puzia T. H., Tsamis Y. G., 2016, ApJ, 825, L16
Müller H. S. P., Thorwirth S., Roth D. A., Winnewisser G., 2001, A&A, 370, 49
Müller H. S. P., Schlöder F., Stutzki J., Winnewisser G., 2005, J. Mol. Struct., 742, 215
Ohlendorf H., Preibisch T., Gaczkowski B., Ratzka T., Grellmann R., McLeod A. F., 2012, A&A, 540, 81
Ossenkopf V., Henning T., 1994, A&A, 291, 943
Ossenkopf V., Krips M., Stutzki J., 2008, A&A, 485, 917
Pickett H. M., Poynter R. L., Cohen E. A., Delitsky M. L., Pearson J. C., Müller H. S. P., 1998, J. Quant. Spec. Radiat. Transf., 60, 883

[5] http://www.astropy.org
[3] https://almascience.nrao.edu/aq/?result_view=observations
[4] https://mast.stsci.edu/portal/Mashup/Clients/Mast/Portal.html

Pineda J. L., Goldsmith P. F., Chapman N., Snell R. L., Li D., Cambrésy L., Brunt C., 2010, ApJ, 721, L686
Povich M. S., et al., 2011, ApJS, 194, 14
Price-Whelan A. M., et al., 2018, AJ, 156, 123
Rathborne J. M., Brooks K. J., Burton M. G., Cohen M., Bontemps S., 2004, A&A, 418, 563
Rebolledo D., et al., 2016, MNRAS, 456, 2406
Rebolledo D., et al., 2020, ApJ, 891, L113
Reiter M., Smith N., 2013, MNRAS, 433, 2226
Reiter M., Smith N., 2014, MNRAS, 445, 3939
Reiter M., Smith N., Bally J., 2016, MNRAS, 463, 4344
Reiter M., Kiminki M. M., Smith N., Bally J., 2017, MNRAS, 470, 4671
Robitaille T., Bressert E., 2012, APLpy: Astronomical Plotting Library in Python, Astrophysics Source Code Library, ascl:1208.017
Robitaille T., Rice T., Beaumont C., Ginsburg A., MacDonald B., Rosolowsky E., 2019, astrodendro: Astronomical data dendrogram creator, Astrophysics Source Code Library, ascl:1907.016
Roccatagliata V., Preibisch T., Ratzka T., Gaczkowski B., 2013, A&A, 554, 6
Rosolowsky E. W., Pineda J. E., Kauffmann J., Goodman A. A., 2008, ApJ, 679, L1338
Schneider N., et al., 2012, A&A, 542, 18
Schöier F. L., van der Tak F. F. S., van Dishoeck E. F., Black J. H., 2005, A&A, 432, 369
Sharda P., Federrath C., da Cunha E., Swinbank A. M., Dye S., 2018, MNRAS, 477, 4380
Smith N., 2006a, MNRAS, 367, 763
Smith N., 2006b, ApJ, 644, L1151
Smith N., Bally J., Walborn N. R., 2010a, MNRAS, 405, 1153
Smith N., et al., 2010b, MNRAS, 406, 952
Tremblin P., Audit E., Minier V., Schneider N., 2012a, A&A, 538, 31
Tremblin P., Audit E., Minier V., Schmidt W., Schneider N., 2012b, A&A, 546, 33
Tremblin P., et al., 2013, A&A, 560, 19
Tychoniec Ł., et al., 2021, A&A, 655, 65
Walch S., Whitworth A. P., Bisbas T. G., Wünsch R., Hubber D. A., 2013, MNRAS, 435, 917
Wilson T. L., Rood R., 1994, ARA&A, 32, 191

APPENDIX A: OPTICAL DEPTH MAPS

Maps of the average and maximum ^{12}CO optical depth are shown in Fig. A1. The median value for the Mystic Mountains and each individual pillar are reported in Table 2.

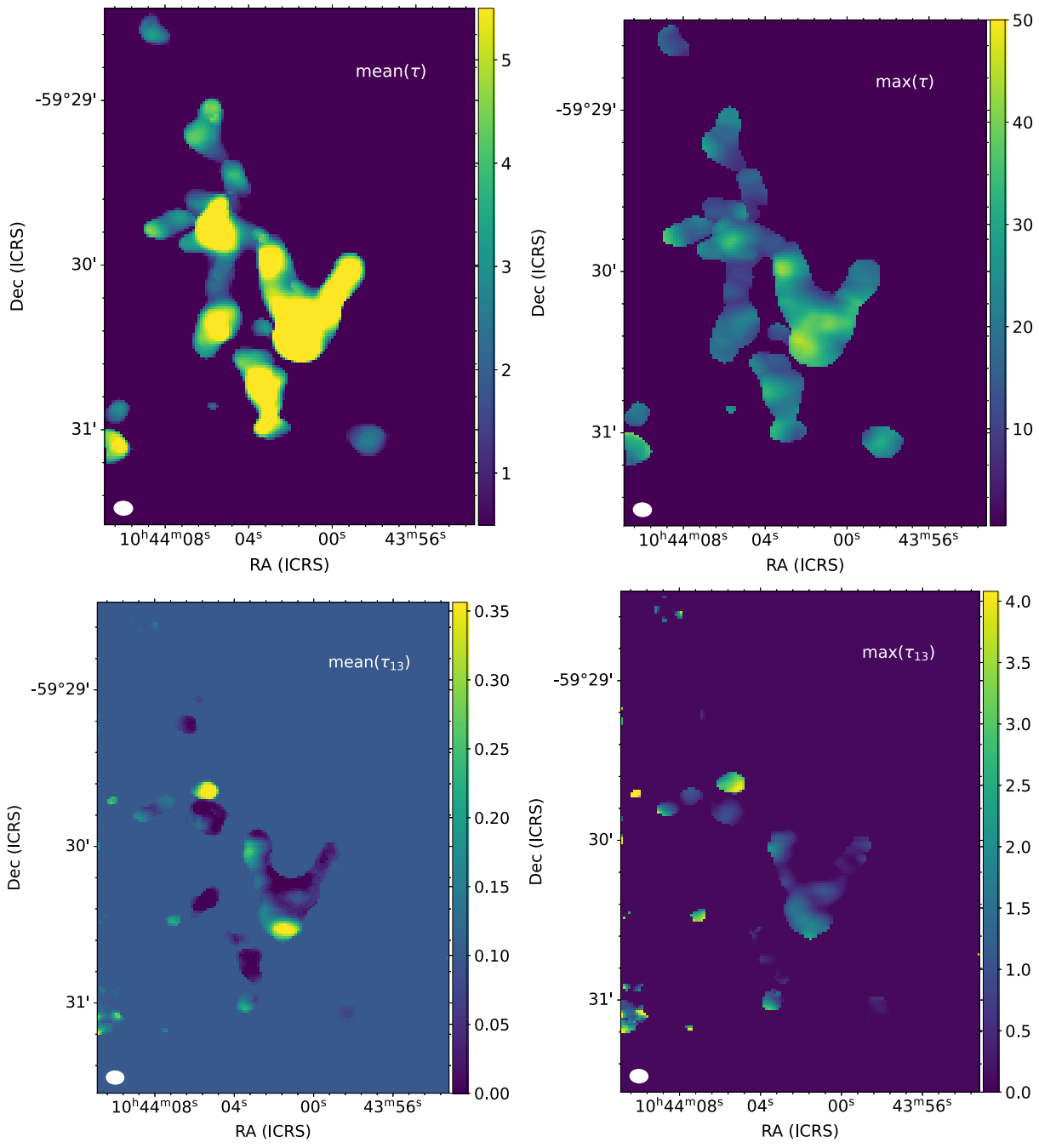

Figure A1. *Left:* the mean and *right:* maximum τ of CO (top) and ^{13}CO (bottom) over the velocity range $-10.5 < v < -2\,\mathrm{km\,s^{-1}}$.

APPENDIX B: COLUMN DENSITY MAPS

The spatially resolved, optical-depth corrected column density of each of the three CO isotopologues is shown in Fig. B1. Peak and median values for the Mystic Mountains and each individual pillar are reported in Table 2.

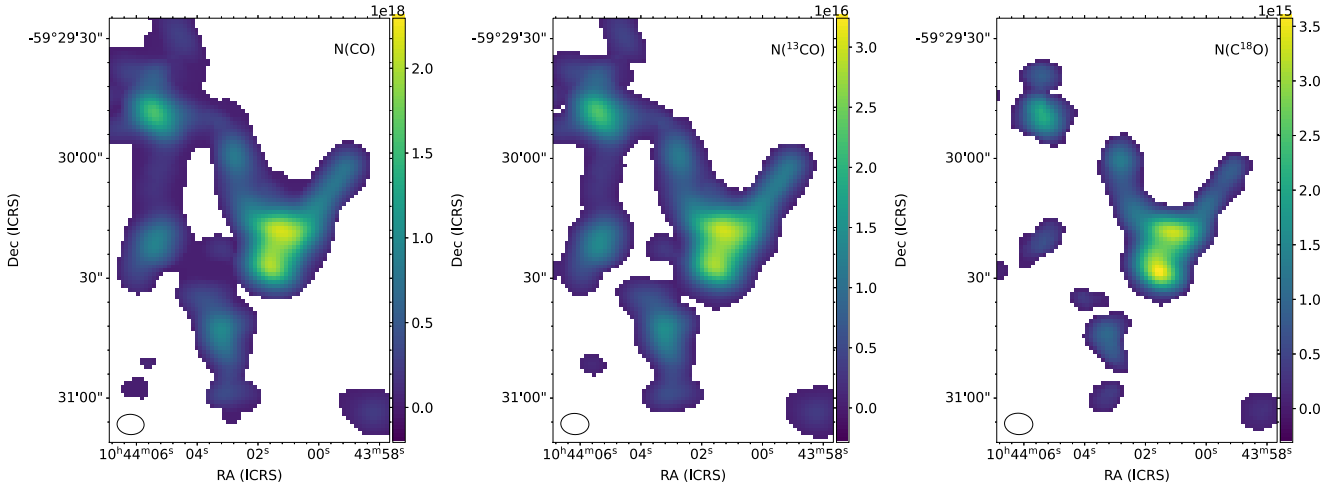

Figure B1. Column density maps of the CO isotopologues over the velocity range $-10.5 < v < -2\,\mathrm{km\,s^{-1}}$.

APPENDIX C: TURBULENCE DRIVING PARAMETER ANALYSIS FOR THE INDIVIDUAL PILLARS

We repeat the analysis in Section 3.8 to isolate turbulent motions in each pillar of the Mystic Mountains complex individually. The pillars in the Mystic Mountains are all at slightly different velocities and these differences are not cleanly removed with a linear gradient. These real velocity differences therefore inflate any measure of the velocity dispersion for the Mystic Mountains as a whole. Ideally, each pillar would be analysed separately to remove these systematic motions.

Figs C1, C2, and C3 show the results of this analysis for the individual pillars and Table C1 reports the derived values with 1σ uncertainties. We find unphysical values for many parameters, including the turbulent driving parameter b. This is almost certainly a reflection of the low resolution of our data compared to the size of the pillars: the width of the HH 901 and HH 1066 pillars are both comparable to the size of the beam.

To test this, we degraded the resolution of the data to 1/4 of the native resolution (as in Sharda et al. 2018). Repeating the analysis, we find that $\sigma_{v,\,3D}$ changes by >20 per cent for the separate pillars. For the Mystic Mountains as a whole, derived values change by $\sim$6 per cent using the lower-resolution data. Formal error propagation does not capture this underlying problem, leading to modest uncertainties on unphysical values in Table C1. A more reliable analysis requires higher angular observations that better resolve the individual pillars.

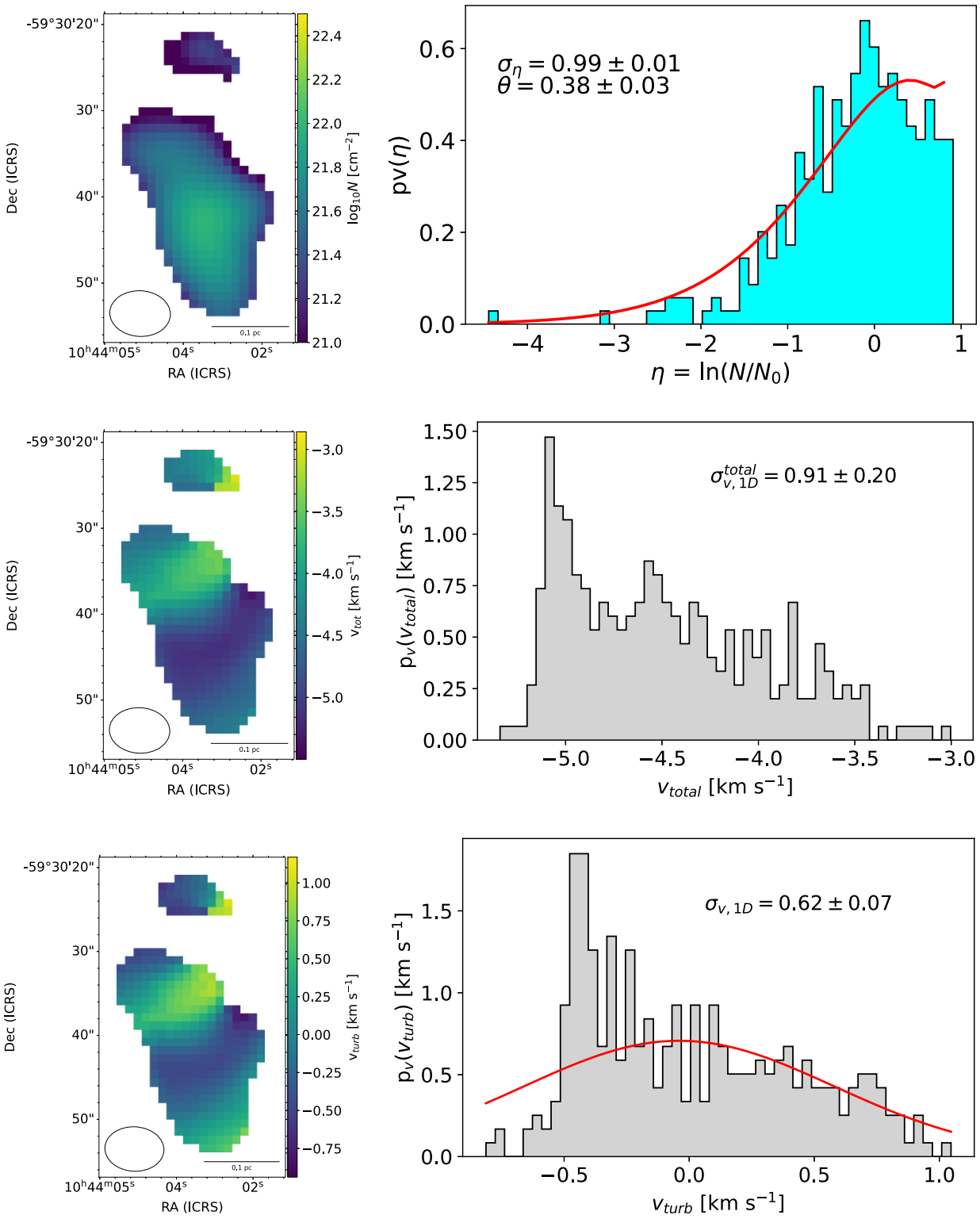

Figure C1. Same as Fig. 14 but for the HH 901 pillar alone.

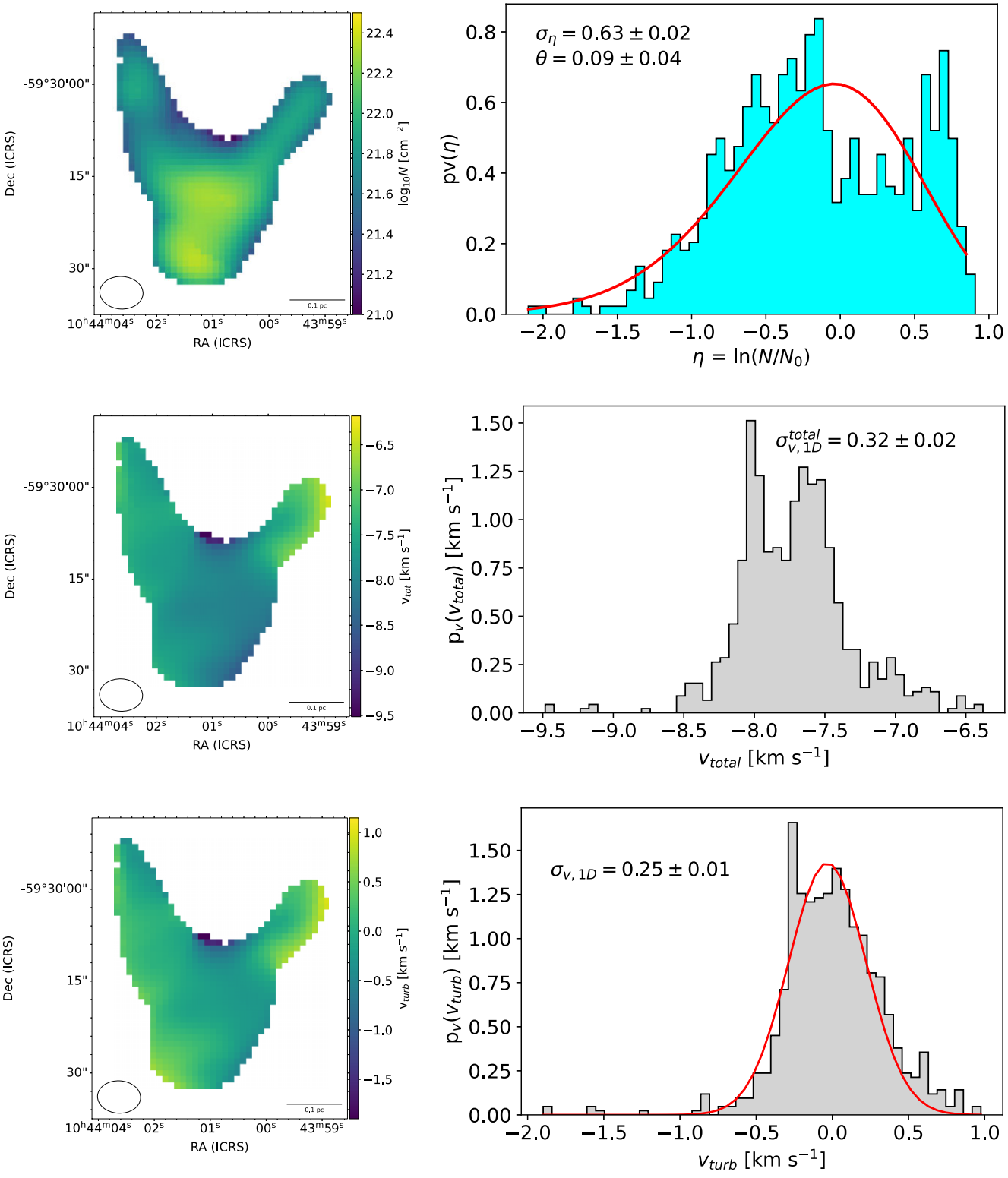

Figure C2. Same as Fig. 14 but for the HH 902 pillar alone.

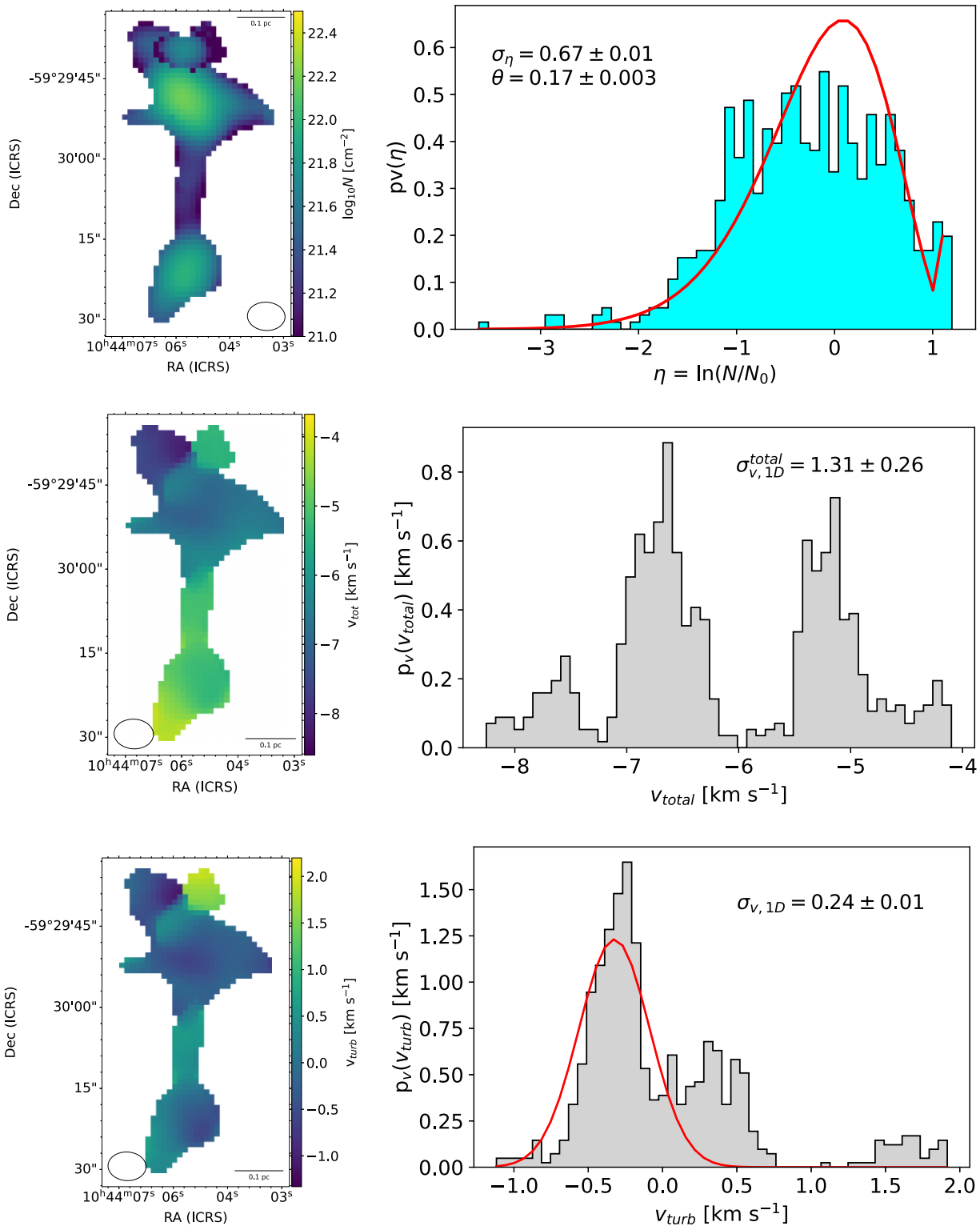

Figure C3. Same as Fig. 14 but for the HH 1066 pillar alone.

Table C1. Turbulence parameters each pillar in the Mystic Mountains individually.

Pillar	HH 901	HH 902	HH 1066
A [pc^2]	0.07 ± 0.007	0.18 ± 0.02	0.20 ± 0.02
N_0 [10^{21} cm^{-2}]	$3.09^{+3.5}_{-1.6}$	$7.59^{+6.0}_{-3.4}$	$3.47^{+4.1}_{-1.9}$
M [M$_\odot$]	3.31 ± 2.64	17.2 ± 13.2	8.13 ± 7.51
n [10^3 cm^{-3}]	4.16 ± 1.06	6.10 ± 0.76	2.95 ± 0.80
$\sigma^{M2}_{v,3D}$ [km s^{-1}]	0.31 ± 0.23	0.27 ± 0.15	0.26 ± 0.26
α_{vir}	16.3 ± 1.90	0.76 ± 0.12	1.24 ± 0.33
t_{ff}/t_{turb}	1.73 ± 0.10	0.37 ± 0.03	0.48 ± 0.06
σ_η	0.99 ± 0.01	0.63 ± 0.02	0.67 ± 0.01
σ_{N/N_0}	0.52 ± 0.01	0.46 ± 0.02	0.45 ± 0.01
$\mathcal{R}^{1/2}$	0.09 ± 0.003	0.13 ± 0.0004	0.09 ± 0.001
σ_{ρ/ρ_0}	5.76 ± 0.21	$3.49 \pm .15$	$4.75 \pm .08$
$\sigma^{\rm total}_{v,1D}$ [km s^{-1}]	0.91 ± 0.20	0.32 ± 0.02	1.31 ± 0.26
$\sigma_{v,\,1D}$ [km s^{-1}]	0.62 ± 0.07	0.25 ± 0.01	0.24 ± 0.01
$\sigma_{v,\,3D}$ [km s^{-1}]	1.07 ± 0.13	0.44 ± 0.02	0.41 ± 0.02
$\mathcal{M}$	3.58 ± 0.43	1.47 ± 0.05	1.38 ± 0.07
b	1.61 ± 0.2	2.37 ± 0.13	3.45 ± 0.19

This paper has been typeset from a TEX/LATEX file prepared by the author.